Butiseaca, G.A.; van der Meer, M.T.J.; Kontakiotis, G.; Agiadi, K.; Thivaiou, D.; Besiou, E.; Antonarakou, A.; Mulch, A.; Vasiliev, I. (2022). Multiple crises preceded the Mediterranean Salinity Crisis: Aridification and vegetation changes revealed by biomarkers and stable isotopes. *Global Planet. Change 217*: 103951.
DOI: 10.1016/j.gloplacha.2022.103951

Multiple crises preceded the Mediterranean Salinity Crisis: Aridification and vegetation changes revealed by biomarkers and stable isotopes

Geanina A. Butiseacă[1,2,3]*, Marcel T.J. van der Meer[4], George Kontakiotis[5], Konstantina Agiadi[6], Danae Thivaiou[5], Evangelia Besiou[5], Assimina Antonarakou[5], Andreas Mulch[1,2], Iuliana Vasiliev[1]

[1]*Senckenberg Biodiversity and Climate Research Centre (SBiK-F), Senckenberganlage 25, D-60325 Frankfurt am Main, Germany*

[2]*Institute of Geosciences, Goethe University Frankfurt, Altenhöferalle 1, 60438, Frankfurt am Main, Germany*

[3]*Eberhard Karls Universität Tübingen, Institute of Archaeological Sciences, Palaeoanthropology Department, Tübingen, Germany*

[4]*Royal Netherlands Institute for Sea Research, Department of Marine Microbiology and Biogeochemistry, P.O. Box 59, 1790 AB, Den Burg, Texel, The Netherlands*

[5]*Faculty of Geology and Geoenvironment, School of Earth Sciences, Department of Historical Geology-Paleontology, National and Kapodistrian University of Athens, Panepistimiopolis, Zografou, 15784, Athens, Greece*

[6]*Department of Palaeontology, University of Vienna, Josef-Holaubek-Platz 2, UZA II, 1090, Vienna, Austria*

*e-mail: butiseacageanina@gmail.com; https://orcid.org/0000-0002-1579-1998

Abstract

During the Messinian (7.24–5.33 Ma), the highly dynamic Mediterranean environment was concomitantly governed by global climate changes and regional tectonic activity affecting the connectivity to the global ocean. The combined effects generated extreme and rapid paleoenvironmental changes culminating in the Messinian Salinity Crisis (MSC; 5.96–5.33 Ma). Here, we reconstruct paleoenvironmental conditions recorded in the Agios Myron section (Crete Island, Greece) between ~7.2 and 6.5 Ma that indicate marked changes affecting the eastern Mediterranean region prior to the onset of the MSC. Hydrogen isotope ratios measured on alkenones produced by haptophyte algae within the Mediterranean water column, coupled to carbon isotopes measured on long chain *n*-alkanes produced by higher terrestrial plants show three important dry periods peaking at 6.98, 6.82 and 6.60 Ma accompanied by shifts in vegetation, transitioning from dominantly C_3 to markedly increased C_4 plants contribution and intermittent recurrence of C_3 vegetation at ~6.99 Ma and 6.78 Ma. Mean annual air temperatures reconstructed using branched glycerol dialkyl glycerol tetraethers (brGDGTs) average 13 °C with an overall pattern that permits orbitally-controlled pacing of the regional climate. Additionally, the branched and isoprenoid tetraether index and bulk carbon and oxygen isotope ratios indicate changes in the source(s) of organic matter and evolution of the basin towards a closed and arid system. These results support a model of ongoing restriction affecting the eastern Mediterranean Sea from ~7 Ma onwards and reveal a protracted aridification of the Mediterranean domain prior to the onset of the MSC.

Keywords: C_4 vegetation expansion, Messinian cooling, ongoing restriction, aridisation, change in organic matter sources, marine-continental decoupling.

1. **Introduction**

The Mediterranean basin hosts some of the best-dated geological sections for the upper Miocene, many of them acting as reference sections for the geological time scale (e.g. Hilgen et al., 1999; 2000; Hüsing et al., 2009). The region has been investigated extensively using micropalaeontology, magnetostratigraphy and radiometric dating, resulting in precise astronomically-tuned sections (e.g. Hilgen et al., 1999; Krijgsman et al., 1999; 2002; Kouwenhoven et al., 2006; Drinia et al., 2007; Zachariasse et al. 2021). However, paleoclimate proxy data embedded within this tight temporal framework are still scarce (e.g. Tzanova et al., 2015; Mayser et al., 2017; Vasiliev et al., 2017; Kontakiotis et al., 2019) and usually focused on the late Messinian with a predominant emphasis on the Messinian Salinity Crisis (MSC; e.g. Vasiliev et al., 2017; Natalicchio et al., 2017; Sabino et al., 2020). Recently, the Agios Myron section (Crete Island, Greece) was biostratigraphically dated and astronomically tuned (Zachariasse et al. 2021). Based on the resulting age model for the early Messinian (~7.2–6.5 Ma), a combined analysis of biomarkers and oxygen isotopes ($\delta^{18}O$) on planktonic foraminifera permitted the reconstruction of sea surface temperature (SST) and associated salinity (SSS) (Kontakiotis, Butiseacă et al., 2022). Consequently, in Agios Myron section, a series of events was identified defining the paleoenvironmental evolution of the eastern Mediterranean between ~7.2–6.5 Ma (Kontakiotis, Butiseacă et al., 2022): during an overall cooling phase 1 (7.2–6.9 Ma), freshening of Mediterranean surface waters (SSS = 38) coincided with the warmest temperatures (SST = 26 °C). Two distinct warm (SST = 29 °C) and hypersaline events (at 6.9–6.82 and 6.72 Ma with SSS = 47 to 48) characterised phase 2 (6.9–6.7 Ma). During phase 3 (6.7–6.5 Ma), increased climatic variability is reflected in a wide range of recorded temperature and salinity values (SST between 23–30 °C and SSS between 37−48).

Here, we build upon the available age model (Zachariasse et al., 2021) and the SST and SSS reconstructions (Kontakiotis, Butiseacă et al., 2022) and provide a comprehensive integration of marine and continental proxy records for the eastern Mediterranean during the pre-MSC Messinian. We achieve this by coupling the existing biomarker record to compound-specific hydrogen (δ^2H) and carbon ($\delta^{13}C$) isotope data that collectively track a complex array of events and reflect the interplay between gateway restriction, basin isolation and orbital oscillations. We analyze changes in the hydrological budget of the Mediterranean basin through 1) δ^2H values from alkenones (produced by haptophyte algae within the Mediterranean Sea surface water), and 2) we track changes in the vegetation surrounding the basin using $\delta^{13}C$ values of *n*-alkanes (originating from higher terrestrial plants). We further reconstruct 3) mean annual air temperatures (MAT) and 4) paleo-soil pH based on branched glycerol dialkyl glycerol tetraethers (brGDGTs), biomarkers produced primarily by soil bacteria in the basin catchment. Additionally, we use the branched and isoprenoid tetraether (BIT) index 5) to detect changes in the source(s) of organic matter. The biomarker data are supplemented by 6) carbon ($\delta^{13}C$) and oxygen ($\delta^{18}O$) isotope ratios measured on bulk sedimentary rocks to monitor the long-term trends in paleoenvironmental conditions affecting the eastern Mediterranean basin. Our results indicate that, in the eastern Mediterranean, the crisis leading to the deposition of the km-thick evaporites in the Mediterranean during the MSC was initiated already during the early Messinian and reflects rather the cumulative effect of successive highly evaporative events progressing in intensity throughout the Messinian, ultimately culminating with the MSC. These events are associated with large-scale aridification and fundamental changes in vegetation composition, a pattern earlier identified throughout the entire North Africa and the Middle East (e.g. Uno et al., 2016; Targhi et al., 2021; Böhme et al., 2021) and now recognised also in the sedimentary record of the eastern Mediterranean.

2. Chronostratigraphy

The ~25-m thick Agios Myron section (N 35°23′ 35.90", E 25°12′67.91") is located in the Heraklion basin (Crete Island, Greece; Fig. 1). The lowest seven meters of the section consist of silty marls without any visually identifiable evidence for cyclic deposition, while the overlying deposits (up to 25 m) show a clear cyclic alternation of blueish-grey homogeneous and brownish laminated marl couplets (the latter referred to here as sapropels) of various thicknesses (Fig. 2). The sedimentary succession is rich in macrofauna, with bivalves being the most abundant (e.g. pycnodonts, cardiids, lucinids, veneriids, pectinids), followed by gastropods (e.g. buccinids), bryozoans, fish and occasionally plant remains mostly preserved in the upper part, where cyclic alternations of homogeneous and laminated marls are visible (Fig. 2).

The present age model is based on the combination of astronomically calibrated planktonic foraminiferal bioevents, tephra layers (Cretan Ash Layers; CAL1–3; Fig. 2) and the midpoints of the sapropels (Zachariasse et al., 2021). The astronomically tuned part of the Agios Myron section covers the 7.05−6.54 Ma time interval. The age control for the four lowermost samples is less well defined in the absence of biostratigraphic events and visible lithological cycles (Zachariasse et al., 2021). However, these four oldest samples were assigned to the earliest Messinian based on the continuous presence of *Globorotalia miotumida*, hence they are considered younger than 7.25 Ma and older than the first astronomically dated sample at 7.05 Ma (Kontakiotis, Butiseacă et al., 2022).

3. Material and methods

3.1. Lipid extraction, fraction separation and analysis

Forty-seven sedimentary rock samples were dried, weighed and ground using agate mortar and pestle. Lipids were extracted using Soxhlets with a mixture of dichloromethane (DCM) and methanol (MeOH) 7.5:1 (*v:v*) and pre-extracted cellulose thimbles. Extracts were evaporated to near dryness under N_2 flow using a TurboVap LV. Subsequently elemental sulphur was removed from the total lipid extracts (TLE) using Cu shreds. Cu was activated using 10% HCl, the acid was then removed and Cu was rinsed with demineralized water until neutral pH was achieved. The Cu was further cleaned using MeOH and DCM. The vials containing TLE, activated Cu and magnetic rods were placed on a rotary table for >16 hours. Afterwards, the TLEs were filtered over a Na_2SO_4 column to remove Cu fragments and water. The remaining solvents were evaporated using N_2. The desulphurization step was repeated until no reaction with the Cu was observed. 10% of the TLE was archived while the rest was further separated into fractions containing different lipids using Al_2O_3 column chromatography. The apolar fraction was eluted using a mixture of *n*-hexane and DCM (9:1, *v:v*), followed by a ketone fraction using DCM, while a mixture of DCM/MeOH (1:1, *v:v*) was used to obtain the polar fraction. The apolar fraction containing *n*-alkanes was purified using $AgNO_3$ column, eluting with *n*-hexane. The ketone fraction containing alkenones was also purified using $AgNO_3$ column by eluting with ethyl acetate. Both *n*-alkanes and alkenones were analyzed and identified based on mass spectra and retention time by Gas Chromatography-Mass Spectrometry (GC-MS) using a Thermo Scientific Trace GC Ultra machine at the Senckenberg Biodiversity and Climate Research Centre (SBiK-F) in Frankfurt am Main, Germany.

3.2 Compound specific stable isotopes analysis

3.2.1 δ^2H *analysis on long chain alkenones* (C_{37} *and* C_{38})

δ^2H values of 21 samples were determined by GC/Thermal Conversion (TC)/ isotope ratio monitoring MS (irMS) using an Agilent GC coupled to a Thermo Electron DELTA$_{Plus}$ XL mass spectrometer at the Royal Netherlands Institute for Sea Research (NIOZ). The alkenone fraction was injected manually on-column on a RTX column of 60 m length, 0.32 mm diameter and 0.25 film thickness. The injection volume was 1.0−1.5 µl, with the TC reactor set at 1425 °C. The H_3^+ -factor was determined daily and was 6.0 ± 0.3 ppm mV^{-1}. Samples were replicated between one to four times depending on the available material, aiming for peaks of >1500 mV for compounds of interest. Hydrogen gas with a predetermined isotopic composition was used as monitoring gas and the isotope values were calibrated against in-house lab standard "Mix B" (A. Schimmelmann; Indiana University). A squalane standard was co-injected with every sample with an average value of −166 ± 0.3‰ over all injections. C_{37} alkenones were integrated as one single peak for obtaining the most accurate value possible.

3.2.2 *$\delta^{13}C$ analysis on long chain n-alkanes (C_{29} and C_{31})*

$\delta^{13}C$ values of individual long chain *n*-alkanes (for 17 samples) were measured on the cleaned apolar fraction using a GC-irMS under similar conditions than the δ^2H measurements, but with a combustion interface rather than thermal conversion. The $\delta^{13}C$ values (expressed relative to V-PDB) were calculated by comparison to a CO_2 reference gas (calibrated against NBS-19). Standard deviations were determined using a co-injected standard and are ± 0.3‰.

3.3 HPLC analysis

3.3.1 *Preparation and analysis*

The polar fraction containing GDGTs was dried under a gentle stream of N_2 then dissolved in a 1-ml mixture of *n*-hexane (*n*-hex)/isopropanol (IPA)-(99:1, *v:v*), slightly dispersed using an ultrasonic bath (up to 30 s per sample) and filtered over a 0.45 mm PTFE filter using a 1 ml syringe. Polar compounds were measured at the Senckenberg-BiK-F laboratory using an HPLC Shimadzu, UFLC performance, Alltech Prevail© Cyano 3 mm, 150−2.1 mm analytical column; eluents *n*-hex (A) and IPA (B) coupled with an ABSciex 3200 QTrap chemical ionization mass spectrometer (HPLC/APCIeMS). We used an injection volume of 5 ml for each sample and GDGTs detection was achieved through single ion monitoring (scanned masses: 1018, 1020, 1022, 1032, 1034, 1036, 1046, 1048, 1050, 1292, 1296, 1298, 1300, 1302). Both isoprenoid and branched GDGTs were analyzed within a single acquisition run for each sample. Quantification was performed using the Analyst software and the peaks were integrated manually for each sample multiple times.

3.3.2 *Mean annual temperature calculation (MAT) and paleo soil pH*

Estimates of continental MAT are based on the relative distribution of brGDGT membrane lipids. The distribution of brGDGTs, expressed as the Methylation index of Branched Tetraethers (MBT) and the Cyclisation ratio of Branched Tetraethers (CBT), displays a significant linear correlation with modern MAT in the range of −6 to 27 ºC (Weijers et al., 2007). For MAT and soil pH calculation, we used the Peterse et al. (2012) calibration, where:

$$MAT' = 0.81 - 5.67 \times CBT + 31 \times MBT'$$

$$pH = 7.90 - 1.97 \times CBT$$

MBT’ and CBT are expressed as:

$$MBT' = [(GDGT\ Ia + GDGT\ Ib + GDGT\ Ic)] / [(GDGT\ Ia + GDGT\ Ib + GDGT\ Ic) + (GDGT\ IIa + GDGT\ IIb + GDGT\ IIIb) + (GDGT\ IIIa)]$$

and

$$\mathrm{CBT} = -\log\,(\mathrm{GDGT\ Ib} + \mathrm{GDGT\ IIb}) / (\mathrm{GDGT\ Ia} + \mathrm{GDGT\ IIa})$$

where GDGT I − GDGT III are branched GDGTs.

3.3.3 *BIT Index*

The BIT (Branched and Isoprenoid Tetraethers) index defines the terrigenous versus aquatic components of organic input into the basin (marine or lacustrine). The BIT index is the ratio of the three major brGDGTs (mostly terrigenous) to isoGDGT Crenarchaeol (aquatic) (Hopmans et al., 2004):

$$\mathrm{BIT} = [(\mathrm{GDGT\text{-}I}) + (\mathrm{GDGT\text{-}II}) + (\mathrm{GDGT\text{-}III})] \,/\, [(\mathrm{Crenarchaeol}) + (\mathrm{GDGT\text{-}I}) + (\mathrm{GDGT\text{-}II}) + (\mathrm{GDGT\text{-}III})]$$

Crenarchaeol is a compound derived from Thaumarchaeota (Sinninghe Damste et al., 2002), accounting for ~20% of the picoplankton in the ocean, although in subordinate abundance it can also occur in soils (Weijers et al., 2007). BrGDGTs occur in high abundances in terrestrial settings, including soils and peats (Hopmans et al., 2004; Peterse et al., 2012). BIT values close to 1 indicate a predominantly terrigenous source, while low values (close to 0) indicate a strong aquatic source of the organic matter (Schouten et al., 2013).

3.4. $\delta^{13}C$ and $\delta^{18}O$ analysis on bulk sedimentary rocks

Samples were dried and drilled with a manual precision drill at the SBiK-F laboratory after being tested with HCl 10% for carbonate presence. The obtained sample powder was weighed and placed into exetainer vials. Isotopic ratios were analyzed at the Goethe University−Senckenberg BiK-F Stable Isotope Facility using a Thermo Scientific MAT 253 mass spectrometer and a Thermo Scientific GasBench II in continuous flow mode, following the protocol of Spötl & Vennemann (2003). All samples were calibrated and measured against standard reference materials (Carrara marble, NBS 18 and Merck). Isotopic values were calculated against a CO_2 reference gas with a precision of 0.06‰ for $\delta^{13}C$ and 0.08‰ for $\delta^{18}O$, respectively. All values are presented with respect to Vienna Pee Dee Belemnite (VPDB).

4. Results

4.1. Compound-specific stable isotopes on biomarkers

4.1.1. δ^2H on long chain alkenones

Alkenones are intermittently present in the section between 7.12 and 6.59 Ma (Fig. 3E). The δ^2H values of C_{37} alkenones (δ^2H_{C37}) vary between −199 and −155‰ (Table 1; Fig. 3E), with an average value of −179‰. Between 7.12 and 7.03 Ma, measured δ^2H_{C37} values vary between –183‰ and –178‰ with an average of –181‰ followed by a first maximum of –155‰ at 6.99−6.98 Ma. Subsequently, δ^2H_{C37} values decrease markedly to –187‰ (at 6.97 Ma). Between 6.97 and 6.83 Ma δ^2H_{C37} remains relatively low except for a short positive excursion at 6.86 Ma (–176‰). At 6.82 Ma, δ^2H_{C37} values increase sharply to –159‰, then decrease progressively until 6.78 Ma to attain an overall minimum of –199‰. At 6.77 Ma, there is another short positive (ca. 30‰) excursion in the δ^2H_{C37} values. Between 6.76−6.65 Ma, δ^2H_{C37} decreases with a mean value of –189‰, after which values increase again up to –157‰ at 6.60 Ma. The interval between 6.87−6.76 Ma registers the largest variability in the section (ca. 40‰). The δ^2H values of C_{38} alkenones (δ^2H_{C38}) follow a similar trend with slightly lower absolute values (Table 1). Samples AM 22 (7.05 Ma) and AM 01C (6.58 Ma) have much higher relative contributions of C_{38} alkenones, therefore we could only measure δ^2H_{C38}.

4.1.2 $\delta^{13}C$ on long chain n-alkanes

The $\delta^{13}C$ values of C_{29} *n*-alkanes ($\delta^{13}C_{C29}$) vary between –34.6‰ and –28.6‰ (Table 2; Fig. 3F), with an average of –32.2‰. Up section, from 7.16 Ma, $\delta^{13}C_{C29}$ values decrease until 6.99 Ma, attaining the minimum value of –34.6‰. We observe a positive excursion at 6.98 Ma to –30.9‰. $\delta^{13}C_{C29}$ values remain relatively low at (avg.) –34.6‰ and reach another maximum of −30.6‰ at 6.83Ma. At 6.78 Ma a brief sharp drop of 2‰ is recorded. Between 6.76 and 6.56 Ma the $\delta^{13}C_{C29}$ remain high and reach a third maximum of –28.6 ‰ at 6.56 Ma. Values of $\delta^{13}C_{C29}$ and $\delta^{13}C_{C31}$ generally co-vary throughout the section (Table 2).

4.2. MAT estimates based on brGDGTs

Measured MAT values range from 6 °C to 21 °C (Table 3; Fig. 3G) with a mean value of 13.4 °C. From ~7.2 Ma to 7.05 Ma MAT values increases gradually (from 14 °C to 21 °C) to reach the overall maximum in the section. From 7.05 to 6.7 Ma, MAT follows an overall cooling trend (from 21 °C to 6 °C), then gently increases to ca. 14 °C until the end of the section.

4.3. Soil pH estimates based on brGDGTs

Paleo-soil pH values in the Agios Myron section increase in a stepwise manner, with values ranging between 5.5 and 7.9 (Table 3; Fig. 3H) and presenting an average value of 6.8. Between 7.16–6.97 Ma the pH is rather constant (~6.8). From 6.95–6.74 Ma its amplitude is increasing, with a variability of 1.4 around an average value of 7.0 with the largest internal variability in the section between 6.72−6.54 Ma.

4.4 BIT Index

The Agios Myron BIT indices are highly variable (Table 3; Fig. 4B) ranging between ~0.26 to ~0.88, indicating input of organic matter from variable sources. From 7.16 to 6.88 Ma, BIT values are higher, ranging between ~0.52 and ~0.86, with a mean value of 0.72. Between 6.87 and 6.80 Ma, BIT values decrease, reaching the lowest of 0.26−0.38. Overall, in this time interval, values are ranging between 0.26 and 0.62, with a mean value of 0.46. From 6.80 Ma until the end of the section at 6.54 Ma, BIT values increase again from ca. 0.59 to 0.88.

The BIT index values vary with lithology, with homogeneous marls generally exhibiting lower values than laminated marls, except couplets AM 18−AM 18C (6.95−6.93 Ma), AM 17−AM 17C (6.93−6.92 Ma), AM 14−AM 14C (6.85−6.84 Ma), AM 11−AM 11C (6.80−6.79 Ma), AM 10−AM 10C (6.77−6.76 Ma) and AM 07−AM 07C (6.70−6.69 Ma) (Fig. 4B).

4.5. Carbon and oxygen isotope ratios of bulk carbonates

The $\delta^{13}C$ record of bulk sedimentary rock material ($\delta^{13}C_{bulk}$) ranges from –1.29‰ to −0.01‰ with an overall average of –0.56‰ (Table 4; Fig. 3C). Between 7.16 and 6.98 Ma, $\delta^{13}C_{bulk}$ values display a rather large variability (–1.23‰ to –0.61‰, average –0.94‰). From 6.97 to 6.82 Ma, $\delta^{13}C_{bulk}$ values display a positive trend from ca –0.65‰ to –0.01‰ (average value of –0.33‰). Between 6.81–6.54 Ma, the $\delta^{13}C_{bulk}$ values show increased variability. The mean value for this interval is –0.59‰, with a minimum of –1.29‰ and a maximum value of 0.01‰, the highest in the entire section. Overall, the $\delta^{13}C_{bulk}$ data show an increasing trend in the lower part of the section up to ~6.8 Ma, followed by a decreasing trend until the end of the record, at 6.54 Ma.

The $\delta^{18}O_{bulk}$ record has a mean value of –0.15‰ and co-varies with $\delta^{13}C_{bulk}$ (Fig. 3D; Table 4). From the base of the section to 6.98 Ma, $\delta^{18}O$ values show an increasing trend and a large variability with values between –2.30‰ and –0.55‰. Between 6.97 and 6.82 Ma, values are increasing up to 0.91‰, most of them being positive. Values have a smaller variability (1.80‰), with an average value of 0.40‰. In the upper part of the section (6.81–6.54 Ma), the isotopic values follow an overall decreasing trend, but with a larger amplitude. Values for this interval vary between –1.64 and 1.30‰, with an average value of –0.16‰.

5. Discussion

During the late Miocene, hydrological conditions in the Mediterranean basin were strongly influenced by the interplay between tectonics promoting gateway restriction and global climate change (e.g. Manzi et al., 2013; Hilgen et al., 2007). Tectonically controlled changes in the basin configuration and ultimately in marine connections (Flecker et al., 2015), led to changes in water circulation patterns, atmospheric circulation and ultimately vegetation and fauna. The initiation of the northern hemisphere glaciation enhanced the climatic changes during the latest Miocene, contributing to a stepwise aridification (Herbert et al., 2016).

5.1 Early Messinian cooling and onset of drier conditions at 7.0 Ma

The Mediterranean climate conditions during the Messinian share similarities with the present day (e.g. Kontakiotis et al., 2019), with dry and hot summers and wet winters (Rohling et al., 2015) and a strong influence of westerlies (Quan et al., 2014). A change in atmospheric circulation patterns from trade winds to westerlies (Quan et al., 2014) during the Tortonian (11.61−7.25 Ma), may have induced weakening of the Asian and African monsoons, and thus a reduction in precipitation amount and an increase in aridity. The expansion of aridity in the Mediterranean area during the late Miocene was also enhanced by changes in circulation patterns in the North Atlantic (Eronen et al., 2012) and Atlantic moisture distribution (Bosmans et al., 2020) as a consequence of restriction of the Betic and Rifian corridors and closure of paratethyan gateways (Pérez-Asensio et al., 2012; Ng et al., 2021 a, b).

In Agios Myron, normal marine conditions prevailed before 7 Ma, with temperatures warmer than present-day sea water. This interval is marked by a 7 °C cooling on SST, from 27.2 °C at 7.17 Ma (sample AM25) to 20.7 °C at 7.03 Ma (sample AM21), accompanied by freshening of the Mediterranean surface waters to 39, with δ^2H_{C37} around −180‰, close to those recorded in the eastern Mediterranean during the glacial-interglacial transition (van der Meer et al., 2007; Fig. 3E). The cooling trend of ~ 7 °C presented in Figure 3 at the lowest part of the study section (earliest Messinian), is correlated with the replacement of *Globorotalia menardii* group with *Globorotalia miotumida* in the planktonic fauna (indicative of cooler conditions; Antonarakou et al., 2004), along with the concurrent decrease of warm-water species (e.g., *G. obliquus*) and minor shifts of cool-water species such as *G. glutinata* and *G. scitula*. For the same interval, the $\delta^{13}C_{n\text{-alkanes}}$ values are indicative of high C_3 plants dominance, with mean annual air temperature on the continent in the range of 16 °C, similar to the present-day situation.

The end of this period, at 7 Ma, is remarkable (Fig. 3). Our δ^2H_{C37} data show a +23‰ shift (from 7.03 to 7.00 Ma; Fig. 3E) in the Agios Myron section, suggesting the onset of an evaporative period at ca. 7 Ma associated with a warming of 5 °C in the marine domain, (Kontakiotis, Butiseacă et. al., 2022). A similar intensity warming episode takes place in the continental domain as well (Fig. 3G), concomitant with increasing $\delta^{13}C_{n\text{-alkanes}}$ values indicative of an increased C_4 plants contribution (Fig. 3F). This dry interval recorded at Agios Myron coincides with the first aridification episodes of the Sahara, when eolian dunes appear in the Chad Basin indicating recurrent desert conditions also starting at ca. 7 Ma (Schuster et al., 2006).

5.2 Hydrological changes in the eastern Mediterranean: Protracted basin isolation between 7.0 and 6.55 Ma

The 7.0 to 6.55 Ma time interval stands out, with δ^2H_{C37} reaching a value of −155‰ at Agios Myron, 30‰ higher than the highest value of −185‰ recorded in the eastern Mediterranean basin (during the glacial-interglacial transition at ~120 ka; van der Meer et al., 2007; Fig. 3E). We interpret these high δ^2H_{C37} values as an expression of recurring enhanced evaporation affecting the Mediterranean basin.

Considering that present-day marine δ^2H_{C37} values are typically below −180‰ (Weiss et al., 2019) (e.g. in the Sargasso Sea at 31º N; Englebrecht and Sachs, 2005), we propose a strongly negative water balance for the Mediterranean Basin, where water loss by evaporation must have outpaced precipitation and river runoff from the basin catchment. Similarly high δ^2H_{C37} values have been reported in regions affected by basin-wide massive evaporation e.g. during the latest phase of the MSC (Vasiliev et al., 2017) or during recurrent droughts affecting the Paratethys-Black Sea region during the late Miocene (Vasiliev et al., 2013, 2015, 2020; Butiseacă et al., 2021). The large (44‰) variation in δ^2H_{C37} values from Agios Myron (Fig. 3E) indicates severe hydrological changes within the Mediterranean Basin between 7.0 and 6.55 Ma, as δ^2H_{C37} values depend mainly on the δ^2H of the water and salinity (Schouten et al., 2005).

Three marked periods characterized by high δ^2H_{C37} values (up to −155‰; Fig. 3E), occur within the Agios Myron section that we interpret to reflect dryer conditions (D1−D3 intervals in Fig. 3). In between these three intervals, δ^2H_{C37} drops to values as low as −199‰, similar to those recorded in present-day open marine environments (Englebrecht and Sachs, 2005; Weiss et al., 2019).

The first interval with high δ^2H_{C37} (D1; $\delta^2H_{37} = -155‰$, centred at ~6.98 Ma; Fig. 3) coincides with relatively high SST (26°C), reduced SSS (~38; Kontakiotis, Butiseacă et al., 2022) and a minor decrease (ca. 0.22‰ and 0.79‰, respectively) in isotopic values to $\delta^{13}C_{bulk} = -1.09‰$ and $\delta^{18}O_{bulk} = -1.79‰$ (Fig. 3 C, D). At the same time, the $\delta^{13}C_{n\text{-alkane}}$ values (Fig. 3F) record a positive shift of ~5‰, consistent with a higher C_4 plant contribution ($\delta^{13}C_{29}$ of −30.9‰), reflecting generally drier conditions concomitant with an increase in MAT values (Fig. 3G). Collectively, these proxy data point to a dry phase (i.e. high δ^2H_{37} and high $\delta^{13}C_{n\text{-alkanes}}$) associated with warm conditions (high SST and MAT) during D1, centered at 6.98 Ma. Reduced salinity in the Mediterranean basin during this interval is consistent with a rather efficient water exchange via the Atlantic gateway(s) and inflow from the Atlantic Ocean outpacing the net evaporative loss, in agreement with the initiation and strengthening of Mediterranean outflow during that time (Ng et al., 2021b).

The second time interval characterized by high δ^2H_{C37} values is centered at 6.82 Ma (D2; with δ^2H_{37} reaching −157‰; Fig. 3E). It is associated with high SST^H (29 °C), high SSS values (~48) and high $\delta^{18}O_{bulk}$ values (Fig. 3C). The essential difference between the first (D1) and this second (D2) period is that salinity values are very high during D2. Additionally, the remarkably similar patterns of SSS^H and $\delta^{18}O_{bulk}$ curves hint that salinity (i.e. evaporation) was the main driver for the changes in the $\delta^{18}O_{bulk}$ values, as these depend (besides the SST) on evaporation (E), precipitation (P) and runoff (R). When E>P+R, the salinity of a restricted basin is increasing, as observed here (Fig. 3). During D2 event all SST, SSS, $\delta^{18}O_{bulk}$ and δ^2H_{C37} indicate high salinity in the aquatic domain (i.e. high evaporation), while on land, the $\delta^{13}C_{n\text{-alkanes}}$ shows values typical of increased C_4 plants contribution, adapted to drier environments. During D2, $\delta^{13}C_{n\text{-alkanes}}$ values are high up to 6.83 Ma and towards the termination of D2 (ca. −31 to −32‰) but drop to as low as −34.4‰ at ca. 6.77 Ma D2 pointing to continental carbon input with a higher C_4 contribution at the beginning and end of D2. All continental proxy data (MAT, $\delta^{13}C_{n\text{-alkanes}}$, pH; Fig. 3) show large variability during D2 similar to the $\delta^{2}H_{37alkenones}$ and $\delta^{13}C_{bulk}$ and $\delta^{18}O_{bulk}$ values, suggesting that this time interval may be characterized by a series of consecutive smaller events (peaking at ~6.78, 6.83 and 6.86 Ma). We propose that this variability within the basin reflects the efficiency of the Atlantic gateway(s), where the basin restriction alternated with increased Atlantic input during sea-level high-stands associated with warm phases. This finding is further supported by parallel evidence of Messinian gateways restriction in the region of the Betic and Rifian corridors, with no evidence of Atlantic connection after 6.9 Ma (Krijgsman et al., 2018). Increasing isolation of the Mediterranean due to tectonics and/or eustacy may have led to increased water residence times, which in combination with basin-wide warming resulted in the slow-down of the thermohaline circulation and the enhancement of water column stratification (Kontakiotis, Butiseacă et al., 2022). The recorded changes from the continental proxies show however a shift towards more C_4 vegetation during a generally continental cooling trend (Figs. 3, 4), suggesting a decoupling between the marine and continental domains.

The beginning of a third dry period (D3) is recorded at 6.60 Ma ($\delta^{2}H_{37} = -157$‰ in Fig. 3E), this time with high variability in both SST and SSS values. The termination of D3 is, however, not properly constrained by our data, because the section ends at 6.54 Ma. Importantly, the high $\delta^{2}H_{C37alkenones}$ values are accompanied by high $\delta^{13}C_{n\text{-alkanes}}$ values (−28.6‰; Fig. 3F), suggesting that a highly evaporative Mediterranean basin coincided with increased C_4 plant contribution in the catchment during D3.

Contrary to the first major evaporitic phase (D1), which took place when salinity was lowest (~38), D2 and D3 are associated with high(er) salinity (~48) and very warm surface waters. Just before the first dry phase (D1), SST values reach a minimum in the section (~20

°C), while the MAT starts to decrease (from 21 to 16 °C), representing probably an expression of the global Messinian cooling event (Fig. 3).

During D2 and D3, our collective data indicate that evaporative conditions in the eastern Mediterranean were associated with warmer surface waters (Fig. 3A; Kontakiotis, Butiseacă et al., 2022) and shifts in vegetation towards more C_4 contribution in the basin catchment (Fig. 3F). This relative increase in evaporation could have been the result of 1) a general warming in the circum-Mediterranean area, 2) a reduced connectivity to the Atlantic Ocean or 3) a more local change in bathymetry (i.e. in Heraklion basin). Interestingly, the MAT (Fig. 3G) data indicate an overall cooling trend, suggesting a decoupling from the generally warm marine domain during D2–D3. A global increase in temperature would be expected to generate uniform warming both in the terrestrial and marine domains. This decoupling could be the result of enhanced water column stratification, which is supported by evidence of Messinian gateway restrictions (Krijgsman et al., 2018; Bulian et. al, 2021). Additionally, it is enhanced by tectonically-controlled changes in the Heraklion basin, where intermittent shallowing/isolation of the basin generates a warmer water column when the water surface is reduced. During the Messinian, the newly formed southern Aegean domain was just as today under the direct influence of the African-Eurasian plate's collision which is forcing the Anatolian microplate to rotate and push towards west (Ketin, 1948). The rotational stress creates transpressional ridges and transtensional basins (Sakellariou et al., 2018), changing thus the local topography and subsequently shaping the entire Aegean and eastern Mediterranean domains. Alongside the general Mediterranean restriction, Zachariasse et al. (2021) identified a change in the bathymetry at Agios Myron location mainly between ~6.78 and 6.6 Ma, from a deeper (~ −500 m) to a shallower (~ −100 m) setting (Zachariasse et al., 2021). Comparing our results with this bathymetric curve (Fig. 4A), we observe that D2 evaporative episode partially correlates with this positive change in the basin topography, indicating a local tectonic overprint as well. The sharp and large change in the calculated paleodepth from 6.60 Ma is considered with caution due to the limitations of the methodological approach of Zachariasse et al. (2021) employed to obtain the bathymetric curve.

A restricted basin system during the deposition of Agios Myron is also supported by the positive covariance between $\delta^{13}C_{bulk}$ and $\delta^{18}O_{bulk}$ data as well as their absolute values (e.g. Leng and Marshall, 2004; Meijers et al., 2020) (Table 4, Supplementary figure). Agios Myron $\delta^{13}C_{bulk}$ and $\delta^{18}O_{bulk}$ data suggest a more restricted, increasingly evaporative system for the upper part of the section, enhanced probably by its position within the Heraklion basin and the Aegean domain, which are considerably shallower than the rest of the eastern Mediterranean due to their location on the european plate margin. As $\delta^{13}C$ bulk values additionally reflect changes in productivity (Li and Ku, 1997), the increase in $\delta^{13}C_{bulk}$ could be indicative of an increase in basin productivity, while the increase in $\delta^{18}O_{bulk}$ points to increased evaporation and consequently increasing salinity. The increased $\delta^{13}C_{bulk}$ and $\delta^{18}O_{bulk}$ values associated with increased SSS values could also be associated with increasingly stagnating bottom waters in the entire eastern Mediterranean after 6.7 Ma (Blanc-Valleron et al., 2002; Kouwenhoven et al., 2006).

5.3 Alkenone production and organic matter sources

The exact alkenone producers for the Agios Myron section are not known, thus we refer to the closest documentation of abundances of coccolithophorids (i.e. alkenone producers) from the time-equivalent record (Pissouri, Cyprus; Kouwenhoven et al., 2006). Similarly to Pissouri, we infer that the best candidates as alkenone producers could have been *Coccolithus pelagicus*, "normal sized" reticulofenestrids, *Helicosphaera carteri* and *Umbilicosphaera* spp.. In the Pissouri section, *Coccolithus pelagicus* appears in small percentages until 6.6 Ma, and only rarely reported afterward. Large sized reticulofenestrids are more abundant until 6.8 Ma, when the highest SSS values are recorded in Agios Myron, while the small sized ones become dominant after 6.8 Ma (Kouwenhoven et al., 2006), when the SSS record in Agios Myron indicates a decrease in salinity, albeit with a large variability (Fig. 3B). Importantly, the largest amplitude in δ^2H_{C37} (of 44‰), centered at 6.82 Ma in Agios Myron, occurs while there is no apparent major change in the assemblage of potential alkenone producers at Pissouri. This observation supports the idea that the changes in our δ^2H_{C37} record are determined by changes in the δ^2H of the Mediterranean water (i.e. evaporation/precipitation) and not by changes in the alkenone producer assemblage.

Major algal blooms (including alkenone producers) are correlated with eutrophication, elemental and nutrients enrichment taking place when increased sediment supply occurs in the basin. The occurrence of alkenones in Agios Myron is limited to the ~7.0−6.6 Ma interval, with no alkenones detected from 6.66 Ma up the top of the section (Fig. 3A, E). The presence of alkenones is discontinuous, pointing to changes in nutrient supplies, productive species or alkenone preservation. Based on the changes in foraminiferal populations more eutrophic conditions are inferred after 6.72 Ma in both the Metochia and Agios Myron sections (Zachariasse et al. 2021). For instance, a nutrient enrichment of subsurface waters through a better developed deep chlorophyll maximum was observed, which led to an explosion of *Globigerina bulloides* group and neogloboquadriniids. Seasonal nutrient inputs could have originated also in the newly formed Saharan dunes, with winter storms bringing dust over the eastern Mediterranean (Lourens et al., 2001) as terrestrial input from North Africa is confirmed at ~7.1 Ma further to the north, in central Greece (Böhme et al., 2017).

The BIT index shows an important change in the source of organic matter at 6.87 Ma (Table 3; Fig. 4B). Between 7.16 to 6.88 Ma and 6.80 to 6.54 Ma, mean BIT values of 0.73 indicate a more terrigenous/soil source of organic matter that contrast BIT indices of 0.46, indicating an dominantly aquatic production for the interval between 6.87 and 6.80 Ma. This observation is consistent with results from Crete (Ploutis section) and Zakynthos (Kalamaki section) indicating a mixed origin of the organic matter during the Late Miocene (Kontakiotis et al., 2020, 2021). The Nile and the Saharan rivers may have served as the main east Mediterranean suppliers of clastic sediments during Tortonian-Messinian (Gladstone et al. 2007), with additional contributions from mainland Greece (Karakitsios et al., 2017), western Anatolia, and the proto-Crete islands due to their proximity and position within the Aegean-Mediterranean domain.

The 6.87–6.80 Ma interval is also associated with increased SSTs, SSSs and higher δ^2H_{C37} values, with low BIT values centered at ~ 6.85 Ma. The low BIT values could indicate that the increasingly dry climate had starved the basin in terrestrial sediment and organic matter input and the BIT reflects only the local (marine) sourced organic matter. Low BIT values correspond to increases in $\delta^{13}C_{n\text{-alkanes}}$ and δ^2H_{C37} because drier conditions and low precipitation lead to low riverine discharge of sediment and organic compounds from land. Another explanation would be a change in elevation or distance from terrestrial source as the Heraklion basin was forming at the time (Fassoulas, 2001). This could have resulted in more riverine/terrigenous input when the basin was in a higher tectonic position/closer to land and more marine/aquatic organic matter production when the basin was deeper (i.e. more available accommodation space). When compared to the reconstructed bathymetry (Zachariasse et al., 2021), we observe that low BIT values (~0.2) from 6.84 correlate with a deepening of ~260 m. It is therefore possible that the terrigenous organic matter input and in-situ production in the basin were affected by the development of the Heraklion basin.

5.4 Early Messinian vegetation changes in the eastern Mediterranean: the emergence of C_4 ecosystems

The $\delta^{13}C_{n\text{-alkane}}$ values of plant waxes reflect the contribution of the main vegetation types, with values of ca. –33‰ for C_3 plants (e.g. trees and shrubs) and –21.7‰ for C_4 plants (e.g. grasses, succulents, halophytes) (O'Leary, 1988; Kohn, 2010). The average –30.3‰ value of $\delta^{13}C_{29\ n\text{-alkanes}}$ in the Agios Myron record indicates input from a C_3-dominated ecosystem, with an overall increasing C_4 contribution towards the top of the section (Table 2; Fig. 3F). We observe two major positive shifts in $\delta^{13}C$ of similar amplitude (~5‰): at 6.99–6.98 Ma (from –33.2 to –28.5‰) and at 6.77–6.76 Ma (from –32.9 to –28.4‰). These two shifts appear at times of marked warming (MAT increase; Fig. 3G) and increased evaporation (higher $\delta^2H_{alkenones}$; Fig. 3E). A third shift seems to occur at 6.56 Ma, as suggested by the AM 01 sample (−28.6‰). However, with only one available data point we cannot asses the complete event.

The first positive shift in $\delta^{13}C_{n\text{-alkanes}}$ at 6.99–6.98 Ma is accompanied by increasing SST, MAT, $\delta^2H_{alkenones}$ (i.e. dryer conditions), higher $\delta^{13}C_{bulk}$ and $\delta^{18}O_{bulk}$, lower pH and low SSS, while the second shift in $\delta^{13}C_{n\text{-alkanes}}$ at 6.77–6.76 Ma is accompanied by an overall decrease in SST and SSS, a pronounced negative excursion in $\delta^2H_{alkenones}$, and increased values of MAT, $\delta^{13}C_{bulk}$ and $\delta^{18}O_{bulk}$. While the MAT, $\delta^{13}C_{bulk}$ and $\delta^{18}O_{bulk}$ values have the same trend in both events, $\delta^2H_{alkenones}$, SST and SSS have opposite trends. The 6.99–6.98 Ma shift in $\delta^{13}C_{n\text{-alkanes}}$ occurs during warm and dryer conditions, while the 6.77–6.76 Ma shift takes place in a wetter period, with lower temperatures on land suggesting different climatic mechanisms. Our data here indicate that overall the continental domain underwent changes in vegetation towards more C_4 contribution over decreasing temperatures.

The large-scale fossil vegetation records support the presence of a mixed flora around the Mediterranean during the early Messinian, dominated by trees (e.g. Zidianakis et al., 2007; Ioakim and Koufos, 2009; Velitzelos et al., 2014), but with an increasing presence of open land vegetation (grasses and sedges) (e.g. Ioakim et al., 2005). Increasing presence of xerophytic elements in the area during the Messinian is documented through pollen (Ioakim et al., 2005; Böhme et al., 2017), attesting the presence of Compositae, Graminae and Amaranthaceae families (including Chenopodiaceae), vegetation characteristic to open and dry environments.

The $\delta^{13}C_{n\text{-alkanes}}$ data presented here offers a first isotope-based reporting of changes towards plants adapted to drier habitats appearing already at ~7 Ma in the Mediterranean region. Similar $\delta^{13}C_{n\text{-alkanes}}$ data from the younger (~6.5 to 5.9 Ma) Cyprus (Mayser et al., 2017) and north Italy (~6.1-5.9 Ma; Sabino et al., 2020) successions follow the expected decrease in C_3 contribution in the benefit of the better adapted C_4 plants for the rest of the Messinian (Fig. 5) as more C_4 vegetation adapted to more arid conditions covered the entire Sahara-Mediterranean-Middle East area for that time (Uno et al., 2016; Böhme et al., 2021).

The 5‰ positive shifts of $\delta^{13}C_{n\text{-alkanes}}$ from Agios Myron section point towards a pronounced physiological response of plants in terms of water intake and environmental stress in general, as a consequence of the new climatic conditions (i.e. a colder and drier northern hemisphere), overimposed by tectonic control (i.e. Atlantic-Mediterranean gateway restriction).

6. The eastern Mediterranean region in the Messinian climatic context

The Agios Myron section (~7.2−6.5 Ma) covers the early Messinian stage and documents a series of precursor events of the MSC. Our data point to a protracted restriction and aridity history of the eastern Mediterranean that was marked by transient periods of episodic dry conditions and accompanying shifts in vegetation in the basin catchment. Although the entire Mediterranean Basin was subjected to restriction as a consequence of the altered Atlantic gateways (e.g. Flecker et al., 2015), Agios Myron is also influenced by the development of the Heraklion basin, which shallows considerably between ~6.85−6.6 Ma Zachariasse et al., 2021). A similar complex overlap between a global/regional (i.e. northern hemisphere glaciation; Atlantic-Mediterranean gateway restrictions) and local signals in marginal basins was also identified in the western Mediterranean Basin (e.g. Bulian et al., 2022).

Agios Myron currently provides the only early Messinian MAT record in the Mediterranean (Fig. 6). Air temperatures vary widely between 6 and 21°C similar to the late Messinian (~6.5−5.9 Ma) Pissouri record (Mayser et al., 2017), where MAT cover a range of 5 °C to 28 °C. Pre- and early Messinian sites of the Paratethys in Russia, Serbia and Bulgaria provide an average MAT value of 14−17°C based on branched GDGTs, pollen and leaf physiology, respectively (Vasiliev et al., 2019; Butiseacă et al., 2021; Ivanov et al., 2002; Utesher et al., 2007), while pollen analysis from the Southern Rifian Corridor (Morocco) (Targhi et al., 2021) indicates MATs of 20−24 °C. Late Messinian MATs from Bulgaria and the Black Sea range between 6 °C and 25 °C with an average of ~16 °C (Ivanov et al., 2021; Vasiliev et al., 2020). Collectively, these data document a remarkable similarity of MAT values between the Mediterranean and Paratethys regions for the Messinian stage.

Overall, biomarker data from Agios Myron (Crete) suggest a decoupling between the marine and continental domains after ~7 Ma, with increased temperatures and salinities offshore and an overall cooling on land (in the catchment of the Mediterranean Basin), probably as a consequence of both tectonics and an orbitally paced climate, as suggested for other sections around the Mediterranean (e.g. Bulian et al., 2022). This development paralleled an increase in C_4 vegetation similar to the observations from the Pissouri section (Cyprus) for the ~6.5−5.9 Ma time interval (Mayser et al. 2017). When compared to the Agios Myron $\delta^{13}C_{C29\textit{n}\text{-alkanes}}$ data, the $\delta^{13}C_{C29\textit{n}\text{-alkanes}}$ values from Pissouri indicate an even higher C_4 contribution (–32.6‰ to –27.1‰) indicating that the expansion of C_4 vegetation continued throughout the Messinian stage in the eastern Mediterranean (Fig. 5). This change in vegetation observed in Agios Myron is associated with a larger-scale aridity induced by global cooling and changes in precipitation patterns (i.e. weakening of the African monsoon, Zhang et al., 2014) and may also be the direct response to intense aridification of the north African continent including the development of the Sahara desert (Schuster et al., 2006), Arabia (Böhme et al., 2021) and Paratethys domain (Vasiliev et al., 2020; Butiseacă et al., 2021), that started ~2 Myr earlier.

The drastic late Miocene changes in climate and tectonics led to the reshaping of the European continent landscapes and the creation of land bridges. These not only favoured the migration of plants but also of new faunal elements, now occupying free ecological niches (Koufos et al., 2005). The same environment facilitated the evolution of primates and appearance of early hominines at ~7.2 Ma (Böhme et al., 2017), indicating that the terrestrial ecosystems adapted easier to the new climatic conditions (i.e. colder and dryer) and their biodiversity was less negatively impacted in comparison to their marine counterparts.

Conclusions

Our integrated biomarker and isotope data from Crete (Greece) support a series of significant environmental changes in the eastern Mediterranean Basin between ~7.2 and 6.5 Ma, confirming increased restriction of the eastern Mediterranean during the early Messinian. $\delta^2H_{C37\ alkenones}$ values indicate two periods with highly evaporative conditions peaking at 6.98 and 6.82 Ma (up to −155‰) and the beginning of a third one at 6.62 Ma (−157‰), associated with increasing SSTs and SSSs that remain high after 6.88 Ma. The highly evaporative intervals are associated with shifts in vegetation. $\delta^{13}C_{C29\mathit{n}\text{-alkanes}}$ indicate important increases in C_4 contribution, between 6.99–6.98 Ma, 6.77–6.76 Ma and from 6.56 Ma, coupled with an overall increasing C_4 vegetation trend during the entire early Messinian, supporting a change in vegetation in the eastern Mediterranean catchment. If during the first $\delta^{13}C_{\mathit{n}\text{-alkanes}}$ shift the marine and continental signals are indicating similar environmental conditions (drier, more

C_4 vegetation), proxies behave differently by the time of the second shift (different $\delta^2H_{alkenones}$, SSTs and SSSs), supporting a decoupling of the marine environment from the continental influence. BIT index values also indicate important changes in the organic matter source between ~6.8−6.6 Ma, suggesting a more terrigenous source which could be translated into a shallowing of the basin under tectonic control. A shallowing of the basin in this time interval and its evolution towards a more enclosed system is also supported by $\delta^{13}C$ and $\delta^{18}O$ data on bulk.

Collectively, the Agios Myron data confirm the presence of restricted conditions in the eastern Mediterranean since the early Messinian and reveal an ongoing isolation and aridification of the Mediterranean domain, both under tectonic (acting mostly over the local accommodation space and regional basin connection) and global climate influence (with great impact over moisture and vegetation).

Acknowledgements

We thank Ulrich Treffert for help in the organic geochemistry laboratory and Jens Fiebig for support in the Goethe University-Senckenberg BiK-F Stable Isotope Facility. This research was financed by the Greek-German collaboration project (IKYDA-DAAD): "Quantification of the environmental changes in the Eastern Mediterranean at the onset of the Messinian Salinity Crisis (Crete-Greece)" (QUANTMES) of IV and VK. Collaboration was made possible through the COST Action CA15103 “Uncovering the Mediterranean salt giant” (MEDSALT) supported by COST (European Cooperation in Science and Technology). Analyses were supported by the DFG grant number 398614017 of IV. GAB transmits special thanks to Ronald van Bommel, Monique Verweij and Jort Ossebaar from NIOZ for help in the stable isotope laboratory.

Figure captions:

Figure 1. Map showing the location of Agios Myron section and Heraklion basin within the Mediterranean domain.

Figure 2. Correlation of Agios Myron section with the precession and isolation curves (Laskar, 2004). The stratigraphic log is bordered by sample names, identified planktonic foraminiferal bioevents, ash layers, as well as field pictures depicting the main lithology and cyclicity (A−C).

Figure 3. Summarized results indicating marine and continental signal inferred by a series of proxies: A) TEX_{86} and U^{K}_{37} SST sea surface temperature (SST^{H} and $U^{K}{}_{37}$; Kontakiotis, Butiseacă et al., 2022) B) Sea surface salinity (SSS^{H}, Kontakiotis, Butiseacă et al., 2022); C) $\delta^{13}C$ on bulk sediments; D) $\delta^{18}O$ on bulk sediments; E) $\delta^{2}H$ on alkenones; F) $\delta^{13}C$ on *n*-alkanes; G) Mean annual temperature (MAT); H) Paleo soil pH derived from GDGTs analysis. Error bars are based on the standard deviation of a series of replicate analyses and indicate standard deviation. S1−S3 indicates the main restriction events observed in the section. With blue arrow are indicated the marine proxies, while with green the continental ones. For clarity, selected sample labels are in light grey while ages are in bold italic numbers. The double arrow in panel E indicates the $\delta^{2}H$ measured on alkenones extracted from sediments of the glacial-interglacial transition at ~120 ka from the Eastern Mediterranean (van der Meer et al., 2007). In the lower side, E represents the shortcut from evaporation, P from precipitation and R from runoff. Remark the periods of excessive evaporation during the D1 to D3 events. $>C_3$, $>C_4$ in F panel indicates the vegetation type.

Figure 4. Stratigraphic log correlated with precession and isolation. Summarized proxies indicating an orbital control over the Agios Myron sediments: A) bathymetric curve (Zachariasse et al., 2021); B) BIT Index; C) Mean annual temperature; D) $\delta^{13}C$ on *n*-alkanes. The yellow squares indicate the carbonate layers, while the green ones the laminated marls/sapropels. Selected sample labels are in light grey while ages are in bold italic numbers.

Figure 5. $\delta^{13}C_{n\text{-alkanes}}$ and MAT Messinian Mediterranean records (Govone, Sabino et al., 2020; Pissouri, Mayser et al., 2017; Agios Myron, this study).

Figure 6. Map showing the distribution of temperature during Messinian: 1. Taman, Panagia (Russia; (Butiseacă et al., 2021); 2. Vidin-Montana (Bulgaria; Ivanov et al., 2002); 3. Kladovo (Serbia; Utesher et al., 2007); 4. Crveni Breg (Serbia; Utesher et al., 2007); 5. Beli Breg (Bulgaria; Ivanov et al., 2021); 6. Taman, Zheleznyi Rog (Russia; Vasiliev et al., 2019a); 7. 380 Site (Black Sea; Vasiliev et al., 2015; 2020); 8. Vegora (N. Greece; Bouchal et al., 2020); 9. Agios Myron (Crete, Greece; this study and Kontakiotis, Butiseacă et al., 2022); 10. Faneromeni (E. Crete, Greece; Kontakiotis et al., 2015); 11. Pissouri (Cyprus; Mayser et al., 2017); 12. Kalamaki (Zakinthos, Greece; Vasiliev et al., 2019b); 13. Monte dei Corvi (Italy; Tzanova et al., 2015); 14. Sorbas (Spain; Mancini et al., 2020); 15. Aïn Lorma (Morocco; Targhi et al., 2021). Basemap modified after Vasiliev et al. (2017). The lower bars are indicating the time lengths of each section. With colors are indicated sections of similar age. Synthesis of Messinian SSTs and MATs records from Mediterranean and Paratethys.

References

Antonarakou, A., Drinia, H., Zachariasse, J.W., 2004. Cyclostratigraphic determination of the replacement of Globorotalia menardii group by Globorotalia miotumida group – A significant climatic change signal. Environmental Micropaleontology, Microbiology and Meiobenthology, 1, 155-175.

Blanc-Valleron, M.-M., Pierre, C., Caulet, J.P., Caruso, A., Rouchy, J.-M., Cespuglio, G., Sprovieri, R., Pestrea, S., Di Stefano, E., 2002. Sedimentary, stable isotope and micropaleontological records of paleoceanographic change in the Messinian Tripoli Formation (Sicily, Italy). Palaeogeogr. Palaeoclimatol. Palaeoecol., 185, 255–286. https://doi.org/10.1016/S0031-0182(02)00302-4

Bouchal, J.M., Güner, T.H., Velitzelos, D., Velitzelos, E., Denk, T., 2020. Messinian vegetation and climate of the intermontane Florina–Ptolemais–Servia Basin, NW Greece inferred from palaeobotanical data: how well do plant fossils reflect past environments? Royal Society Open Science 7: 192067. http://dx.doi.org/10.1098/rsos.192067

Butiseacă, G.A., Vasiliev, I., van der Meer, M.T.J., Krijgsman, W., Palcu, D.V., Feurdean, A., Niedermeyer, E.M., Mulch., A., 2021. Severe late Miocene droughts affected Eurasia. Global and Planetary Change, 206, 103644 https://doi.org/10.1016/j.gloplacha.2021.103644.

Böhme, M., Spassov, N., Ebner, M., Geraads, D., Hristova, L., Kirscher, U., Kötter, S., Linnemann, U., Prieto, J., Roussiakis, S., Theodorou, G., Uhlig, G., Winklhofer, M., 2017. Messinian age and savannah environment of the possible hominin *Graecopithecus* from Europe. PLOS ONE 12(5): e0177347. https://doi.org/10.1371/journal.pone.0177347

Böhme, M., Spasov, N., Majidifard, M.R., Gärtner, A., Kirscher, U., Marks, M., Dietzel, C., Uhlig, G., El Atfy, H., Begun, D.R., Winklhofer, M., 2021. Neogene hyperaridity in Arabia drove the direction of mammalian dispersal between Africa and Eurasia. Nature Communications Earth & Environment, 2:85. https://doi.org/10.1038/s43247-021-00158-y

Bosmans, J.H.C., van der Ent, R.J., Haarsma, R.J., Drijfhout, S.S., Hilgen, F.J., 2020. Precession and obliquity induced changes in moisture sources for enhanced precipitation over the Mediterranean Sea. Paleoceanography and Paleoclimatology, 35 (1). https://doi.org/10.1029/2019PA003655

Drinia, H., Antonarakou, A., Tsaparas, N., Kontakiotis, G., 2007. Palaeoenvironmental conditions preceding the Messinian Salinity Crisis: A case study from Gavdos Island. Geobios, 40, 251–265.

Englebrecht, A.C., Sachs J.P., 2005. Determination of sediment provenance at drift sites using hydrogen isotopes and unsaturation ratios in alkenones. Geochim. Cosmochim. Acta, 69, 4253−4265. https:/doi.org/10.1016/j.gca.2005.04.011

Eronen, J.T., Fortelius, M., Micheels, A., Portmann, F.T., Puolamäki, K., Janis, C.M., 2012. Neogene aridification of the Northern Hemisphere. Geology 40:823-826https://doi.org/10.1130/G33147.1

Fassoulas, C., 2001. The tectonic development of a Neogene basin at the leading edge of the active European margin: the Heraklion basin, Crete, Greece. Journal of Geodynamics, 31, 49-70. https://doi.org/10.1016/S0264-3707(00)00017-X

Flecker, R., Krijgsman, W., Capella, W., de Castro, M.C., Dmitrieva, E., Mayser, J.P., Marzocchi, A., Modestu, S., Ochoa, D., Simon, D., Tulbure, M., van den Berg, B., van der Schee, M., de Lange, G., Ellam, R., Govers, R., Gutjahr, M.,,Hilgen F., Kouwenhoven, T., Lofi, J., Meijer, P., Sierro, J.F., Bachiri, N., Barhoun, N., Alami A.C., Chacon, B., Flores, J.A., Gregory, J., Howard, J., Lunt, D., Ochoa, M., Pancost, R., Vincent, S., Yousfi, M.Z., 2015. Evolution of the late Miocene Mediterranean-Atlantic gateways and their impact on regional and global environmental change. Earth-Science Reviews, 150, 365−392. https://doi.org/10.1016/j.earscirev.2015.08.007

Gladstone, R., Flecker, R., Valdes, P.J., Lunt, D., Markwick, P., 2007. The Mediterranean hydrologic budget from a Late Miocene global climate simulation. Palaeogeography, Palaeoclimatology and Palaeoecology, 251, 254–267. https://doi.org/10.1016/j.palaeo.2007.03.050

Hilgen, F.J., Krijgsman, W., 1999. Cyclostratigraphy and astrochronology of the Tripoli diatomite Formation (pre-evaporite Messinian, Sicily, Italy). Terra Nova, 11, 16–22. https://doi.org/10.1046/j.1365-3121.1999.00221.x

Hilgen, F.J., Iaccarino, S., Krijgsman, W., Villa, G., Langereis, C.G.,Zachariasse, W.J. 2000. The global boundary stratotype section and point (GSSP) of the Messinian stage 841 (uppermost Miocene). Episodes, 23, 172–178. 842 https://doi.org/10.18814/epiiugs/2000/v23i3/004

Hilgen, F., Kuiper, K., Krijgsman, W., Snel, E., van der Laan, E., 2007. Astronomical tuning as the basis for high resolution chronostratigraphy: the intricate history of the Messinian Salinity Crisis Stratigraphy, 4 (2–3) 231−238.

Hopmans, E.C., Weijers, J.W.H., Schefuss, E., Herfort, L., Sinninghe Damsté, J.S., Schouten, S., 2004. A novel proxy for terrestrial organic matter in sediments based on branched and isoprenoid tetraether lipids. Earth and Planetary Science Letters, 224, 107–116. https://doi.org/ 10.1016/j.epsl.2004.05.012

Hüsing, S. K., Kuiper, K. F., Link, W., Hilgen, F. J., Krijgsman, W., 2009. The upper Tortonian–lower Messinian at Monte dei Corvi (Northern Apennines, Italy): Completing a Mediterranean reference section for the Tortonian Stage. Earth and Planetary Science Letters, 282 (1–4), 140–157. https://doi.org/10.1016/j.epsl.2009.03.010

Ioakim, C., Rondoyanni, T., Mettos, A., 2005. The Miocene Basins of Greece (Eastern Mediterranean) from a palaeoclimatic perspective. Revue de Paléobiologie, 24, 2.

Ioakim, C., Koufos, G.D., 2009. The late Miocene mammal faunas of the Mytilinii Basin, Samos Island, Greece: new collection. 3. Palynology. In: Koufos, G.D., Nagel, D. (Eds.), The Late Miocene Mammal Faunas of Samos. Beiträge zur Paläontologie, 31, 27–35.

Ivanov., D.A., Ashraf, A.R., Mosbrugger, V., Palmarev, E., 2002. Miocene microflora and paleoclimate reconstructions from three sites in Bulgaria. Pangaea. https://doi.org/10.1594/PANGAEA.596352

Ivanov, D., Utescher, T., Djorgova, N., Bozukov, V., Ashraf, A.R., 2020. The late Miocene Beli Breg Basin (Bulgaria): paleoecology and climate reconstructions based on pollen data. Paleobiodiversity and Palaeoenvironments 101, 79−102. https://doi.org/10.1007/s12549-020-00475-8

Karakitsios, V., Cornée, J.-J., Tsourou, T., Moissette, P., Kontakiotis, G., Agiadi, K., Manoutsoglou, E., Triantaphyllou, M., Koskeridou, E., Drinia, H., Roussos, D., 2017. Messinian salinity crisis record under strong freshwater input in marginal, intermediate, and deep environments: The case of the North Aegean. Palaeogeogr., Palaeoclimatol., Palaeoecol., 485, 316–335, https://doi.org/10.1016/j.palaeo.2017.06.023.

Ketin, I., 1948. Über die tektonisch-mechanischen Folgerungen aus den grossen anatolischen Erdbeben des letzten Dezenniums. Geol Rundsch 36, 77–83.

Kim, J.H., van der Meer, J., Schouten, S., Helmke, P., Willmott, V., Sangiorgi, F., Koç, N., Hopmans E.C., Sinnighe Damsté, J.S., 2010. New indices and calibrations derived from the distribution of crenarchaeal isoprenoid tetraether lipids: Implications for past sea surface temperature reconstructions. Geochimica Et Cosmochimica Acta, 74(16). https://doi.org/10.1016/j.gca.2010.05.027

Krijgsman, W., Hilgen, F.J., Raffi, I., Sierro, F.J., Wilson, D.S., 1999. Chronology, causes and progression of the Messinian salinity crisis. Nature, 400, 652−655. https://doi.org/10.1038/23231

Krijgsman, W., 2002. The Mediterranean: Mare Nostrum of earth sciences. Earth and Planetary Science Letters 205, 1–12.

Krijgsman, W., Capella, W., Simon., D., Hilgen, F.J., Kouwenhoven, T.J., Meijer, P.T., Sierro, F.J., Tulbure., M.A., van der Berg, B.C.J., van der Schee, M., Flecker, R., 2018. The Gibraltar Corridor: Watergate of the Messinian Salinity Crisis. Marine Geology 403, 238–246. https://doi.org/10.1016/j.margeo.2018.06.008

Kohn, M.J., 2010. Carbon isotope compositions of terrestrial C_3 plants as indicators of (paleo)ecology and (paleo)climate. Proceedings of the National Academy of Sciences of the United States of America 107, 19691–19695. https://doi.org/10.1073/pnas.1004933107

Kontakiotis, G., Besiou, E., Antonarakou, A., Zarkogiannis, S.D., Kostis, A., Mortyn, P.G., Moisette, P., Cornée, J.-J., Schulbert, C., Drinia, H., Anastasakis, G., Karakitsios, V., 2019. Decoding sea surface and paleoclimate conditions in the eastern Mediterranean over the Tortonian-Messinian Transition. Palaeogeography, Palaeoclimatology, Palaeoecology, 534. https://doi.org/10.1016/j.palaeo.2019.109312

Kontakiotis, G., Karakitsios, V., Cornée, J.-J., Moissette, P., Zarkogiannis, S.D., Pasadakis, N., Koskeridou, E., Manoutsoglou, E., Drinia, H., Antonarakou, A., 2020. Preliminary results based on geochemical sedimentary constraints on the hydrocarbon potential and depositional environment of a Messinian sub-salt mixed siliciclastic-carbonate succession onshore Crete (Plouti section, eastern Mediterranean). Med. Geosc. Rev. 2, 247–265. https://doi.org/10.1007/s42990-020-00033-6

Kontakiotis, G., Karakitsios, V., Maravelis, A.G., Zarkogiannis, S.D., Agiadi, K., Antonarakou, A., Pasadakis, N., Zelilidis, A., 2021. Integrated isotopic and organic geochemical constraints on the depositional controls and source rock quality of the Neogene Kalamaki sedimentary successions (Zakynthos Island, Ionian Sea). Med. Geosc. Rev. 3, 193–217. https://doi.org/10.1007/s42990-020-00045-2.

Kontakiotis, G., Butiseacă, G.-A., Karakitsios, V., Antonarakou, A., Zarkogiannis, S., Agiadi, K., Krsnik, E., Besiou, E., Zachariasse, J.-W., Lourens, L., Thivaiou, D., Koskeridou, E., Moissette, P., Mulch, A., Vasiliev., I., 2022. Hypersalinity accompanies tectonic restriction in the eastern Mediterranean prior to the Messinian Salinity Crisis. Palaeogeography, Palaeoclimatology, Palaeoecology 592(2):110903. https://doi.org/10.1016/j.palaeo.2022.110903

Koufos, G.D., Kostopoulos, D., Vlachou, T.D., 2005. Neogene/Quaternary mammalian migrations in Eastern Mediterranean. Belgian Journal of Zoology, 135 (2), 181−190.

Kouwenhoven, T.J., Morigi, C., Negri, A., Giunta, S., Krijgsman, W., Rouchy, J.M., 2006. Paleoenvironmental evolution of the eastern Mediterranean during the Messinian:

Constraints from integrated microfossil data of the Pissouri Basin (Cyprus). Marine Micropaleontology 60, 17−44. https://doi.org/10.1016/j.marmicro.2006.02.005

Laskar, J., Robutel, P., Joutel, F., Gastineau, M., Correia, A. C. M., & Levrard, B. 2004. A long-term numerical solution for the insolation quantities of the Earth. Astronomy & Astrophysics, 428, 261–285. https://doi.org/10.1051/0004-6361:20041335.

Leng, M.J., and Marshall, J.D., 2004, Palaeoclimate interpretation of stable isotope data from lake sediment archives. Quaternary Science Reviews, 23, 811–831. https://doi .org/10.1016/j.quascirev.2003.06.012

Li, H.-C., and Ku, T.-L., 1997, $\delta^{13}C$–$\delta^{18}C$ covariance as a paleo hydrological indicator for closed-basin lakes. Palaeogeography, Palaeoclimatology, Palaeoecology, 133, 69–80. https:// doi.org/10.1016/S0031-0182(96)00153-8

Lourens, L.J., Wehausen, R., Brumsack, H.J., 2001. Geological constraints on tidal dissipation and dynamical ellipticity of the Earth over the past three million years. Nature 409, 1029 – 1033. https://doi.org/10.1038/35059062

Mancini, A.M., Gennari, R., Ziveri, P., Mortyn, P.G., Stolwijk, D.J., Lozar, F., 2020. Calcareous nannofossil and foraminiferal trace element records in the Sorbas Basin: A new piece of the Messinian Salinity Crisis onset puzzle. Palaeogeography, Palaeoclimatology, Palaeoecology 554. https://doi.org/10.1016/j.palaeo.2020.109796

Manzi, V., Gennari, R., Hilgen, F., Krijgsman, W., Lugli, S., Roveri, M., Sierro, F.J., 2013. Age refinement of the Messinian salinity crisis onset in the Mediterranean.Terra Nova, 25 (4) 315 – 322. https://doi.org/10.1111/ter.12038

Mayser, J.P., Flecker, R., Marzocchi, A., Kouwenhoven, T., Lunt, D., Pancost, R., 2017. Precession driven changes in terrestrial organic matter input to the Eastern Mediterranean leading up to the Messinian Salinity Crisis. Earth and Planetary Science Letters, 462, 199-211. https://doi.org/10.1016/j.epsl.2017.01.029

Meijers, M.J.M., Brocard, G.Y., Whitney, D.L., Mulch, A., 2020. Paleoenvironmental conditions and drainage evolution of the Central Anatolian lake system (Turkey) during late Miocene to Pliocene surface uplift. GEOSPHERE, 16 (2), 490-509. https://doi.org/10.1130/GES02135.1

Müller, P.J., Kirst, G., Ruhland, G., von Storch, I., Rosell-Mele, A., 1998. Calibration of the alkenone paleotemperature index U-37(K') based on core-tops from the eastern South Atlantic and the global ocean (60˚N–60˚S). Geochim. Cosmochim. Acta, 62, 1757–1772.

Natalicchio, M., Birgel, D., Peckman, J., Carnevale, G., Liu, X., Hinrichs, K.-U., Dela Pierre, F., 2017. An archaeal biomarker record of paleoenvironmental change across the onset of the Messinian salinity crisis in the absence of evaporites (Piedmont Basin, Italy). Organic Geochemistry 113, 242−253. https://doi.org/10.1016/j.orggeochem.2017.08.014

Ng, Z.L., Hernández-Molina, F.J., Duarte, D., Sierro, F.J., Ledesma, S., Rogerson, M., Llave, E., Roque, C., Manar, M.A., 2021a. Latest Miocene restriction of the Mediterranean Outflow Water: a perspective from the Gulf of Cádiz. Geo-Marine Letters 41 (23). https://doi.org/10.1007/s00367-021-00693-9

Ng, Z.L., Hernández-Molina, F.J., Duarte, D., Sierro, F.J., Roque, C., Manar, M.A., 2021b. Late Miocene contourite depositional system of the Gulf of Cádiz: The sedimentary signature of the paleo-Mediterranean Outflow Water. Marine Geology 442. https://doi.org/10.1016/j.margeo.2021.106605

O'Leary, M.H., 1988. Carbon Isotopes in Photosynthesis. BioScience 38, 328–336. http://doi.org/10.2307/1310735

Pérez-Asensio, J.N., Aguirre, J., Schmiedl, G., Civis, J., 2012. Impact of restriction of the Atlantic-Mediterranean gateway on the Mediterranean Outflow Water and eastern

Atlantic circulation during the Messinian. Paleoceanograpgy 27 (3). https://doi.org/10.1029/2012PA002309

Peterse, F., van der Meer, J., Schouten, S., Weijers, J.W.H., Fierer, N., Jacckson, R.B., Kim, J.-H., Sinninghe Damsté, J.S., 2012. Revised calibration of the MBT-CBT paleotemperature proxy based on branched tetraether membrane lipids in surface soils. Geochimica et Cosmochimica Acta, 96:215–229. https://doi.org/10.1016/j.gca.2012.08.011

Quan, C., Liu, Y.-S., Tang, H., Utescher, T., 2014. Miocene schift of European atmospheric circulation from trade wind to westerlies. Scientific Reports 4, 5660. https://doi.org/10.1038/srep05660

Rohling, E.J., Marino, G., Grant, K.M., 2015. Mediterranean climate and oceanography, and the periodic developments of anoxic events (sapropels). Earth-Science Reviews, 143, 62−97. https://doi.org/10.1016/j.earscirev.2015.01.008

Roussiakis, S., Filis, P., Sklavounou, S., Giaourtsakis, I., Kargopoulos, N., Theodorou, G., 2019. Pikermi: a classical European fossil mammal geotope in the spotlight. European Geologist Journal, 48.

Sabino, M., Schefuß, E., Natalicchio M., Dela Pierre, F., Birgel, D., Bortels, D., Schnetger, B., & Peckmann, J., 2020. Climatic and hydrologic variability in the northern Mediterranean across the onset of the Messinian salinity crisis. Palaeogeography, Palaeoclimatology, Palaeoecology, 545, 109632. https://doi.org/10.1016/j.palaeo.2020.109632

Sakellariou, D., Rousakis, G., Morfis, I., Panagiotopoulos, I., Ioakim, C., Trikalinou, G., Tsampouraki-Kraounaki K., Kranis H., Karageorgis A., 2018. Deformation and kinematics at the termination of the North Anatolian Fault: the North Aegean Trough horsetail structure. Proceedings of the 9th International INQUA Meeting on Paleoseismology, Active Tectonics and Archeoseismology, 25−27 June 2018, Possidi.

Schouten, S., Hopmans, E.C., Sinninghe Damsté, J.S., 2013. The organic geochemistry of glycerol dialkyl glycerol tetraether lipids: A review. Organic Geochemistry 54, 19–61. doi:10.1016/j.orggeochem.2012.09.006.

Schouten, S., Ossebar, J., Schreiber, K., Kienhuis, M.V.M., Langer, G., Bijma, J., 2005. The effect of temperature and salinity on the stable hydrogen isotopic composition of long chain alkenones produced by *Emiliania huxleyi* and *Gephyrocapsa oceanica*. Biogeosciences Discussions, 2 (6), 1681–1695. https://bg.copernicus.org/articles/3/113/2006/

Schuster, M., Duringer, P., Ois Ghienne, J.-F., Vignaud, P., Mackaye, H.T., Likius, A., Brunet, M., 2006. The age of Sahara Desert. Science, 311. http://doi.org/10.1126/science.1120161

Sierro, F.J., Flores, J.A., Zamarreño, I., Vásquez, a., Utrilla, R., Francés, G., Hilgem, F.J., Krijgsman, W., 1999. Messinian pre-evaporite sapropels and precession-induced oscillations in western Mediterranean climate. (1999) Marine Geology, 153 (1-4), pp. 137-146. 10.1016/S0025-3227(98)00085-1

Sinninghe Damsté, J.S., Schouten, S., Hopmans, E.C., van Duin, A.C.T., Geenevasen, J.A.J., 2002. Crenarchaeol: the characteristic core glycerol dibiphytanyl glycerol tetraether membrane lipid of cosmopolitan pelagic crenarchaeota. Journal of lipid research 43 (10), 1641-1651. 10.1194/jlr.m200148-jlr200

Spötl, C., Vennemann, T.W., 2003. Continous-flow isotope ratio mass spectrometric analysis of carbonate minerals. Rapid Communications in Mass Spectrometry17, 1004-1006. http://doi.org/ 10.1002/rcm.1010

Targhi, S., Barhoun, N., Taoufiq, B.N., Achab, M., Ait Salem, A., Yousfi, M.Z., 2021. Vegetation climate and marine environmental reconstruction in the western Mediterranean (southern Rifian corridor, Morocco) over the Tortonian-Messinian transition. Helyon 7, 208569. https://doi.org/10.1016/j.heliyon.2021.e08569

Tzanova, A., Herbert, T., Peterson, L., 2015. Cooling Mediterranean Sea surface temperatures during the Late Miocene provide a climate context for evolutionary transitions in Africa and Eurasia. Earth and Planetary Science Letters. 419. http://doi.org/10.1016/j.epsl.2015.03.016

Uno, K.T., Polissar, P.J., Jackson, K.E., deMenocal, P.B., 2016. Neogene biomarker record of vegetation change in eastern Africa. Proceedings of the National Academy of Sciences, 113(23), 6355–6363. https://doi.org/10.1073/pnas.1521267113

Utescher, T., Djordjevic- Milutinovic, D., Bruch, A., Mosbrugger, V., 2007. Paleoclimate and vegetation change in Serbia during the last 30 Ma. Palaeogeography, Palaeoclimatology, Palaeoecology 253, 157–168. https://doi.org/10.1016/j.palaeo.2007.03.037

Van der Meer, M.T.J., Sangiorgi, F., Baas, M., Brinkhuis, H., Sinninghe Damsté, J.S., Schouten, S., 2007. Molecular isotopic and dinoflagellate evidence for Late Holocene freshening of the Black Sea. Earth and Planetary Science Letters 267 (3−4), 426−434. http://doi.org/ 10.1016/j.epsl.2007.12.001

Vasiliev, I., Mezger, E. M., Lugli, S., Reichart, G. J, Manzi, V., & Roveri, M., 2017. How dry was the Mediterranean during the Messinian Salinity Crisis? Palaeogeography, Palaeoclimatology, Palaeoecology, 471, 120–133. https://doi.org/10.1016/j.palaeo.2017.01.032

Vasiliev, I., Reichart, G.J., Krijgsman, W., Mulch, A., 2019. Black Sea rivers capture drastic change in catchment-wide mean annual temperature and soil pH during the Miocene-to-

Pliocene transition, Global and Planetary Change, 172, 428–439. https://doi.org/10.1016/j.gloplacha.2018.10.016

Vasiliev, I., Feurdean, A., Reichart, G.J., Mulch, A., 2020. Late Miocene intensification of continentality in the Black Sea Region. International Journal of Earth Sciences, 109, 831–846. https://doi.org/10.1007/s00531-020-01832-w

Velitzelos, D., Bouchal, J.M., Denk, T., 2014. Review of the Cenozoic floras and vegetation of Greece. Review of Palaeobotany and Palynology 204, 56-117. https://doi.org/10.1016/j.revpalbo.2014.02.006

Weiss, G.M, Schouten, S., Sinninghe-Damsté, J.S., van der Meer, M.T.J., 2019. Constraining the application of hydrogen isotopic composition of alkenones as a salinity proxy using marine surface sediments. Geochimica et Cosmochimica Acta, 250, 34–48. https://doi.org/10.1016/j.gca.2019.01.038

Weijers, J.W.H., Schouten, S., van der Donker, J., Hopmans E.C., Sinninghe Damsté, J., 2007. Environmental controls on bacterial tetraether membrane lipid distribution in soils. Geochimica et Cosmochimica Acta 71, 703–713. https://doi.org/10.1016/j.gca.2006.10.003

Zachariasse, W.J., Kontakiotis, G., Lourens, L.J., Antonarakou, A., 2021. The Messinian of Agios Myron (Crete, Greece): a key to better understanding diatomite formation south of Crete, on Gavdos Island. Palaeogeography, Palaeoclimatology, Palaeoecology, 581, 110633. https://doi.org/10.1016/j.palaeo.2021.110633

Zhang, Z., Ramstein, G., Schustre, M., Li, C., Contoux, C., Yan, Q., 2014. Aridification of the Sahara desert caused by Tethys Sea shrinkage during the Late Miocene, Nature, 513, 401. https://doi.org/10.1038/nature13705

Zidianakis, G., Mohr, B.A.R., Fassoulas, C., 2007. A late Miocene leaf assemblage from Vrysses, western Crete, Greece, and its paleoenvironmental and paleoclimatic interpretation. Geodiversitas 29, 351–377.

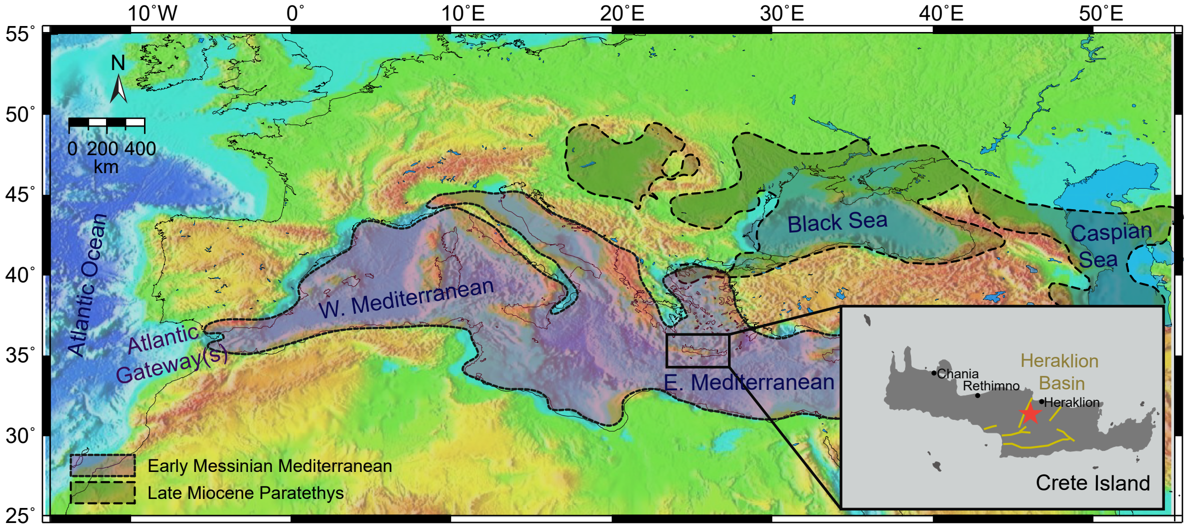

10˚W
0˚
10˚E
20˚E
30˚E
40˚E
50˚E
55˚
50˚
45˚
40˚
35˚
30˚
25˚
N
0 200 400
km
Atlantic Ocean
Atlantic
Gateway(s)
W. Mediterranean
E. Mediterranean
Black Sea
Caspian
Sea
Heraklion
Basin
Chania
Rethimno
Heraklion
Crete Island
Early Messinian Mediterranean
Late Miocene Paratethys

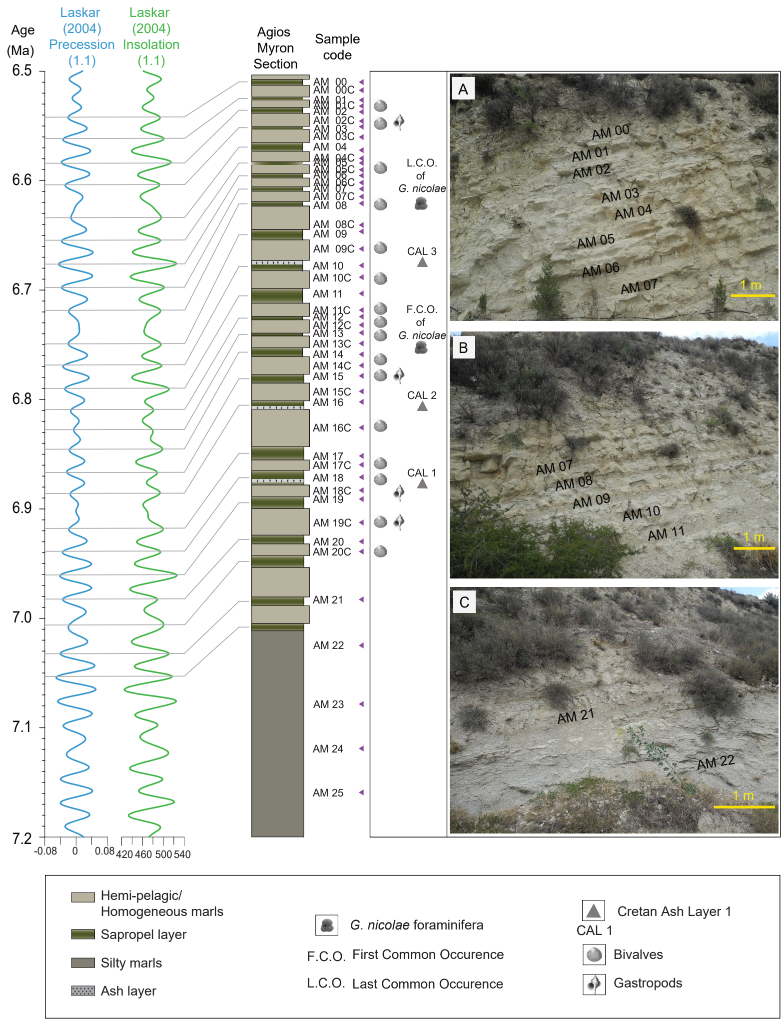

Age (Ma)
Laskar (2004) Precession (1.1)
Laskar (2004) Insolation (1.1)
Agios Myron Section
Sample code
6.5
6.6
6.7
6.8
6.9
7.0
7.1
7.2
-0.08
0
0.08
420 460 500 540
AM 00
AM 00C
AM 01
AM 01C
AM 02
AM 02C
AM 03
AM 03C
AM 04
AM 08
AM 08C
AM 09
AM 09C
AM 10
AM 10C
AM 11
AM 11C
AM 12
AM 12C
AM 13
AM 13C
AM 14
AM 14C
AM 15
AM 15C
AM 16
AM 16C
AM 17
AM 17C
AM 18
AM 18C
AM 19
AM 19C
AM 20
AM 20C
AM 21
AM 22
AM 23
AM 24
AM 25
L.C.O. of G. nicolae
CAL 3
F.C.O. of G. nicolae
CAL 2
CAL 1
A
AM 00
AM 01
AM 02
AM 03
AM 04
AM 05
AM 06
AM 07
1 m
B
AM 07
AM 08
AM 09
AM 10
AM 11
1 m
C
AM 21
AM 22
1 m
Hemi-pelagic/ Homogeneous marls
Sapropel layer
Silty marls
Ash layer
G. nicolae foraminifera
F.C.O. First Common Occurence
L.C.O. Last Common Occurence
Cretan Ash Layer 1 CAL 1
Bivalves
Gastropods

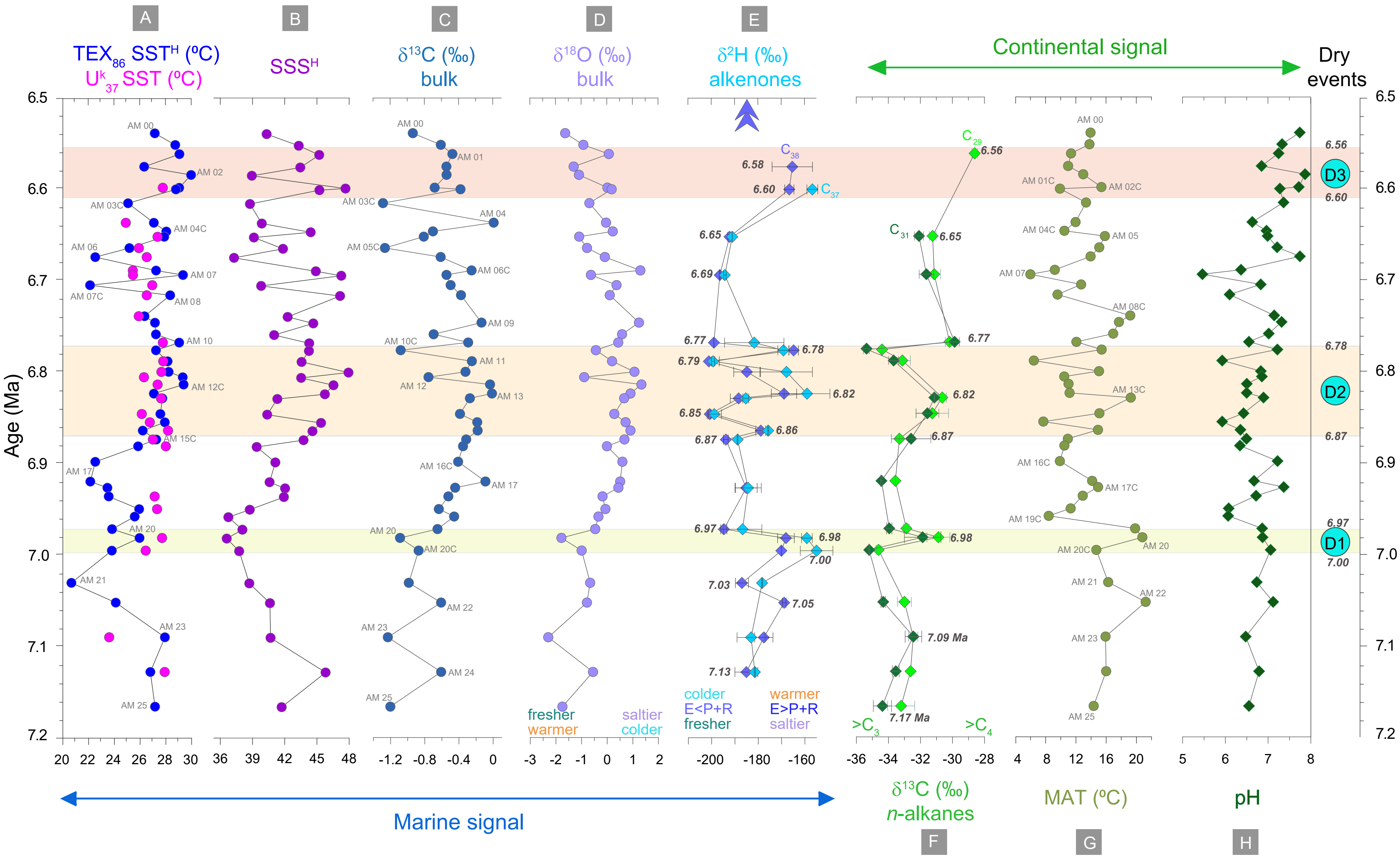

A
B
C
D
E
TEX86 SSTH (ºC)
Uk37 SST (ºC)
SSSH
δ13C (‰) bulk
δ18O (‰) bulk
δ2H (‰) alkenones
Continental signal
Dry events
Age (Ma)
D3
D2
D1
fresher
warmer
saltier
colder
colder
E<P+R
fresher
warmer
E>P+R
saltier
>C3
>C4
Marine signal
δ13C (‰) n-alkanes
MAT (ºC)
pH
F
G
H

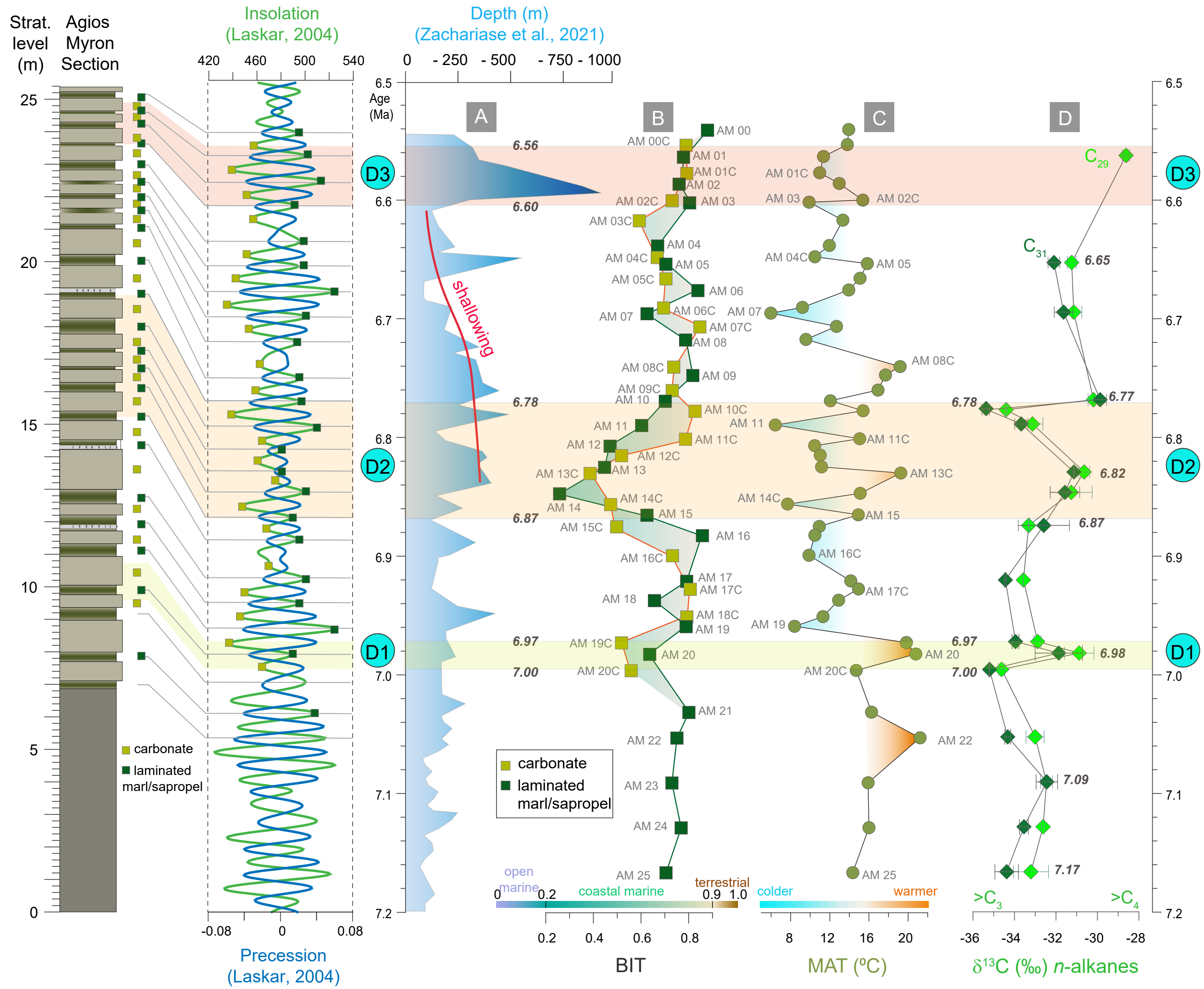

Strat. level (m)
Agios Myron Section
Insolation (Laskar, 2004)
Precession (Laskar, 2004)
Depth (m) (Zachariase et al., 2021)
Age (Ma)
shallowing
A
B
C
D
D3
D2
D1
carbonate
laminated marl/sapropel
open marine
coastal marine
terrestrial
colder
warmer
BIT
MAT (ºC)
δ13C (‰) n-alkanes
C29
C31
>C3
>C4

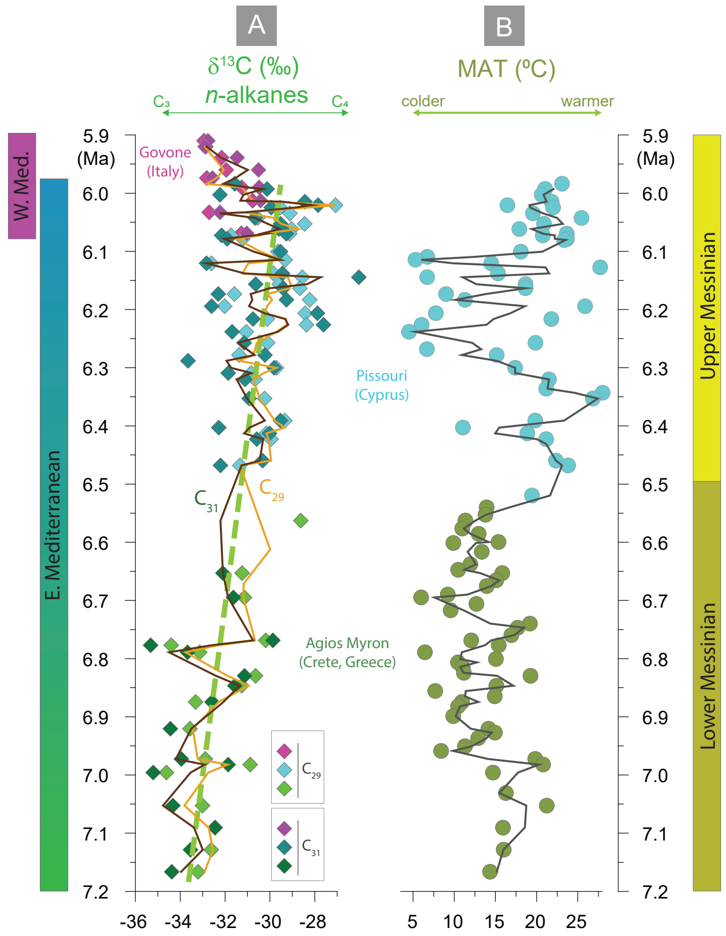
A
B
δ13C (‰)
n-alkanes
C3
C4
MAT (ºC)
colder
warmer
W. Med.
E. Mediterranean
Govone
(Italy)
Pissouri
(Cyprus)
Agios Myron
(Crete, Greece)
C31
C29
Upper Messinian
Lower Messinian
5.9
(Ma)
6.0
6.1
6.2
6.3
6.4
6.5
6.6
6.7
6.8
6.9
7.0
7.1
7.2
-36
-34
-32
-30
-28
5
10
15
20
25

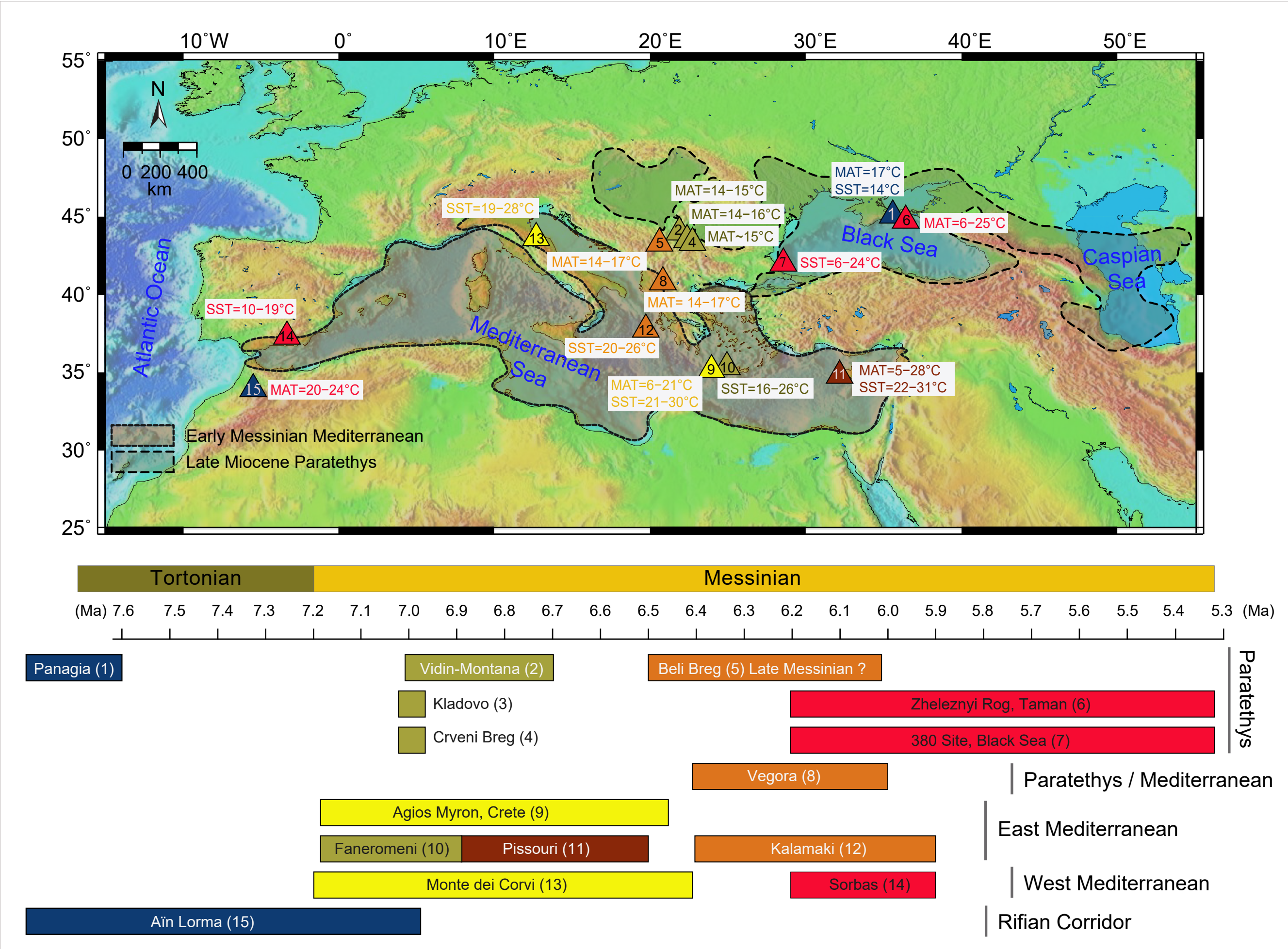

No.	Site	Age (Ma)	MAT (°C)	Method	SST (°C)	Method	Location	Reference
1	Taman, Panagia	7.6	~17	MBT−CBT	14	TEX_{86}	E. Paratethys (Russia)	Butiseacă et al., 2021
2	Vidin-Montana	~7−6.7	14−17	Pollen			C. Paratethys (Bulgaria)	Ivanov et al., 2002
3	Kladovo	~7	14−15	Leaf physionomy			C. Paratethys (Serbia)	Utesher et al., 2007
4	Crveni Breg	~7	14−17	Leaf physionomy			C. Paratethys (Serbia)	Utesher et al., 2007
5	Beli Breg	Late Messinian	~15	Pollen			C. Paratethys (Bulgaria)	Ivanov et al., 2021
6	Taman, Zheleznyi Rog	6.2−5.33	7−18	MBT−CBT			E. Paratethys (Russia)	Vasiliev et al., 2019
7	380 Site	6.2−5.33	6−24	MBT−CBT	16−21	TEX_{86}	E. Paratethys (Black Sea)	Vasiliev et al., 2020; Vasiliev et al., 2015
8	Vegora	6.4−6	10−14	Pollen & leaves			Paratethys/Med. (Greece)	Bouchal et al., 2020
9	Agios Myron	7.2−6.54	6−21	MBT−CBT	21−30	TEX_{86}, U^{K}_{37}	E. Mediterranean (Greece)	**This study**; Kontakiotis, Butiseacă et al., 2022
10	Faneromeni	7.2−6.9			16−26	Sr/Ca	E. Mediterranean (Greece)	Kontakiotis et al., 2019
11	Pissouri	6.9−6.5	5−28	MBT−CBT	22−31	TEX_{86}	E. Mediterranean (Cyprus)	Mayser et al., 2017
12	Kalamaki	6.4−5.9			20−26	U^{K}_{37}	E. Mediterranean (Greece)	Vasiliev et al., 2019
13	Monte dei Corvi	7.2−6.4			19−28	U^{K}_{37}	C. Mediterranean (Italy)	Tzanova et al., 2015
14	Sorbas	6.2−5.9			10−19	Mg/Ca	W. Mediterranean (Spain)	Mancini et al., 2020
15	Aïn Lorma	7.8−7	20−24	Pollen			Rifian Corridor (Morocco)	Targhi et al., 2021

Supplementary material online to accompany

Multiple crises preceded the Mediterranean Salinity Crisis: Aridification and vegetation changes revealed by biomarkers and stable isotopes

by

Geanina A. Butiseacă *, Marcel T.J. van der Meer, George Kontakiotis, Konstantina Agiadi, Danae Thivaiou, Evangelia Besiou, Assimina Antonarakou, Andreas Mulch, Iuliana Vasiliev

*e-mail: butiseacageanina@gmail.com

Supplementary figure and tables

__Supplementary figure:__

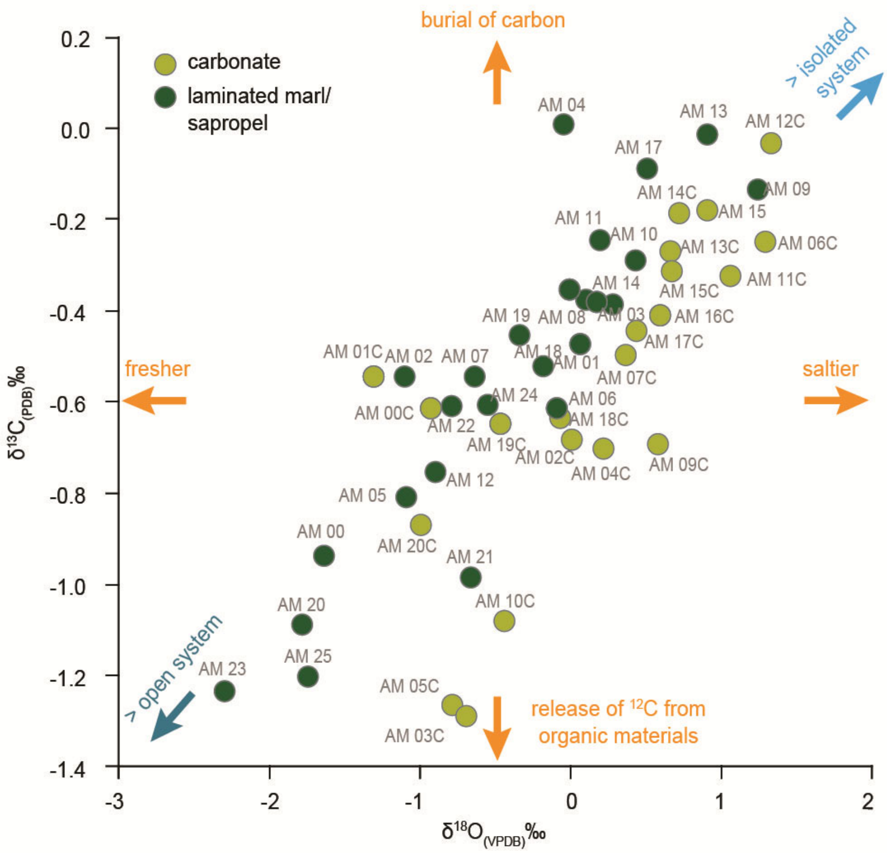

Supplementary figure 1. Diagram showing the distribution of $\delta^{13}C$ against $\delta^{18}C$ on bulk sediments.

Supplementary tables:

Sample Name	Stratigraphic level (m)	Age (Ma)	δ^2H_{C37}	St. dev. δ^2H_{C37}	$N\delta^2H_{C37}$	δ^2H_{C38}	St. dev. δ^2H_{C38}	$N\delta^2H_{C38}$
AM 01C	24.40	6.58	n.d.	n.d.	n.d.	-165.4	8.7	2
AM 03	23.75	6.60	-156.8	2.3	2	-166.7	2.0	2
AM 05	22.50	6.65	-191.2	0.0	2	-192.3	0.8	2
AM 07	21.65	6.69	-194.3	0.5	2	-196.5	0.2	2
AM 10	19.20	6.77	-181.7	12.8	2	-199.0	0.0	2
AM 10C	18.80	6.78	-169.2	2.4	3	-164.9	2.1	2
AM 11	18.20	6.79	-199.4	0.7	2	-201.2	4.5	2
AM 11C	17.70	6.80	-167.9	11.1	2	-184.9	5.6	2
AM 13	16.90	6.82	-159.1	9.8	2	-169.0	5.4	2
AM 13C	16.50	6.83	-185.4	1.3	2	-188.4	3.6	2
AM 14	16.15	6.85	-198.9	3.0	2	-200.8	0.5	2
AM 15	15.45	6.86	-175.7	0.2	2	-178.9	2.1	2
AM 15C	15.00	6.87	-188.9	0.2	2	-193.9	1.0	2
AM 17C	12.55	6.93	-184.4	5.6	2	-185.2	4.7	2
AM 19C	10.65	6.97	-186.8	8.3	2	-194.8	1.3	2
AM 20	10.10	6.98	-159.1	2.3	2	-168.1	3.6	2
AM 20C	9.65	7.00	-155.0	7.0	3	-170.1	0.0	1
AM 21	8.05	7.03	-178.4	0.2	2	-187.0	2.8	2
AM 22	7.10	7.05	n.d.	n.d.	n.d.	-168.9	0.8	2
AM 23	5.50	7.09	-183.1	6.0	2	-177.6	3.9	2
AM 24	3.90	7.13	-181.5	0.2	2	-185.1	4.9	2

Supplementary table 1. δ^2H long chain alkenones (C_{37}−C_{38}) on samples from Agios Myron section.

Sample Name	Stratigraphic level (m)	Age (Ma)	$\delta^{13}C_{C29}$	St. dev. $\delta^{13}C_{C29}$	$N\delta^2C_{C29}$	$\delta^{13}C_{C31}$	St. dev. $\delta^{13}C_{C31}$	$N\delta^{13}C_{C31}$
AM 01	24.65	6.563	-28.6	0.2	2	n.d.	n.d.	n.d.
AM 05	22.50	6.653	-31.2	0.2	2	-32.1	0.3	2
AM 07	21.65	6.695	-31.1	0.4	3	-31.6	0.5	3
AM 10	19.20	6.769	-30.2	0.3	3	-29.9	0.3	3
AM 10C	18.80	6.777	-34.4	0.0	2	-35.3	0.1	2
AM 11	18.20	6.789	-33.1	0.5	2	-33.7	0.3	2
AM 13C	16.50	6.830	-30.6	0.3	2	-31.1	0.0	2
AM 14	16.15	6.847	-31.3	1.0	3	-31.6	0.7	3
AM 15C	15.00	6.874	-33.3	0.0	2	-32.6	1.2	2
AM 17	12.80	6.920	-33.6	0.0	2	-34.4	0.0	2
AM 19C	10.65	6.972	-32.9	0.2	2	-34.0	0.2	2
AM 20	10.10	6.982	-30.9	0.7	3	-31.9	1.1	3
AM 20C	9.65	6.996	-34.6	0.1	2	-35.2	0.0	2
AM 22	7.10	7.053	-33.0	0.4	2	-34.3	0.1	2
AM 23	5.50	7.090	-32.5	0.3	2	-32.4	0.5	2
AM 24	3.90	7.128	-32.6	0.1	2	-33.5	0.2	2
AM 25	2.30	7.166	-33.2	0.8	2	-34.4	0.6	2

Supplementary table 2. δ^{13}C on long chain *n*-alkanes (C_{29}−C_{31}).

Sample Name	Stratigraphic level (m)	Age (Ma)	MAT (°C)	pH	BIT Index
AM 00	25.25	6.54	13.9	7.7	0.88
AM 00C	24.90	6.55	13.8	7.3	0.79
AM 01	24.65	6.56	11.4	7.2	0.78
AM 01C	24.40	6.58	11.0	6.8	0.79
AM 02	24.20	6.59	13.0	7.9	0.76
AM 02C	23.80	6.60	15.4	7.7	0.73
AM 03	23.75	6.60	9.9	7.3	0.80
AM 03C	23.40	6.62	13.3	7.4	0.59
AM 04	22.90	6.64	12.0	6.6	0.67
AM 04C	22.65	6.65	10.5	7.0	0.67
AM 05	22.50	6.65	15.8	7.0	0.70
AM 05C	22.25	6.67	15.1	7.2	0.70
AM 06	22.05	6.68	13.9	7.7	0.84
AM 06C	21.75	6.69	9.2	6.4	0.69
AM 07	21.65	6.69	6.0	5.5	0.63
AM 07C	21.40	6.71	12.7	6.8	0.85
AM 08	21.15	6.72	9.6	6.1	0.79
AM 08C	20.40	6.74	19.2	7.1	0.74
AM 09	20.15	6.75	17.7	7.3	0.82
AM 09C	19.60	6.76	16.9	7.0	0.73
AM 10	19.20	6.77	12.1	6.6	0.70
AM 10C	18.80	6.78	15.4	7.2	0.83
AM 11	18.20	6.79	6.4	5.9	0.60
AM 11C	17.70	6.80	15.1	6.8	0.79
AM 12	17.45	6.81	10.5	6.9	0.47
AM 12C	17.20	6.81	11.0	6.5	0.52
AM 13	16.90	6.82	11.2	6.5	0.45
AM 13C	16.50	6.83	19.3	6.9	0.39
AM 14	16.15	6.85	15.1	6.4	0.26
AM 14C	15.80	6.86	7.7	5.9	0.47
AM 15	15.45	6.86	14.9	6.4	0.62
AM 15C	15.00	6.87	10.9	6.5	0.50
AM 16	14.65	6.88	10.5	6.3	0.86
AM 16C	13.85	6.90	9.9	7.2	0.73
AM 17	12.80	6.92	14.1	6.7	0.79
AM 17C	12.55	6.93	14.9	7.4	0.81
AM 18	12.20	6.94	12.9	6.7	0.66
AM 18C	11.70	6.95	11.3	6.1	0.79
AM 19	11.40	6.96	8.4	6.1	0.79
AM 19C	10.65	6.97	19.8	6.9	0.52
AM 20	10.10	6.98	20.8	6.9	0.64
AM 20C	9.65	7.00	14.7	7.1	0.56
AM 21	8.05	7.03	16.3	6.7	0.80
AM 22	7.10	7.05	21.2	7.1	0.75
AM 23	5.50	7.09	15.9	6.5	0.73
AM 24	3.90	7.13	16.0	6.8	0.77
AM 25	2.30	7.17	14.3	6.6	0.70

Supplementary table 3. MAT, BIT and paleo-pH data obtained from GDGTs.

Sample Name	Stratigraphic level (m)	Age (Ma)	$\delta^{13}C$ (PDB)	$\delta^{18}O$ (VPDB)	N
AM 00	25.25	6.54	-0.94	-1.64	3
AM 00C	24.90	6.55	-0.61	-0.93	4
AM 01	24.65	6.56	-0.48	0.06	3
AM 01C	24.40	6.58	-0.55	-1.31	4
AM 02	24.20	6.59	-0.54	-1.10	7
AM 02C	23.80	6.60	-0.68	0.01	7
AM 03	23.75	6.60	-0.38	0.17	4
AM 03C	23.40	6.62	-1.29	-0.69	7
AM 04	22.90	6.64	0.01	-0.05	7
AM 04C	22.65	6.65	-0.70	0.22	7
AM 05	22.50	6.65	-0.81	-1.09	4
AM 05C	22.25	6.67	-1.27	-0.79	7
AM 06	22.05	6.68	-0.61	-0.09	7
AM 06C	21.75	6.69	-0.25	1.30	7
AM 07	21.65	6.69	-0.55	-0.64	4
AM 07C	21.40	6.71	-0.50	0.36	7
AM 08	21.15	6.72	-0.38	0.10	3
AM 09	20.15	6.75	-0.14	1.24	4
AM 09C	19.60	6.76	-0.70	0.58	4
AM 10	19.20	6.77	-0.29	0.43	4
AM 10C	18.80	6.78	-1.08	-0.44	3
AM 11	18.20	6.79	-0.25	0.19	7
AM 11C	17.70	6.80	-0.32	1.06	4
AM 12	17.45	6.81	-0.76	-0.90	4
AM 12C	17.20	6.81	-0.04	1.34	7
AM 13	16.90	6.82	-0.01	0.91	4
AM 13C	16.50	6.83	-0.27	0.66	4
AM 14	16.15	6.85	-0.39	0.28	4
AM 14C	15.80	6.86	-0.19	0.72	7
AM 15	15.45	6.86	-0.18	0.91	4
AM 15C	15.00	6.87	-0.32	0.67	4
AM 16	14.65	6.88	-0.35	-0.01	7
AM 16C	13.85	6.90	-0.41	0.59	7
AM 17	12.80	6.92	-0.09	0.51	3
AM 17C	12.55	6.93	-0.44	0.44	7
AM 18	12.20	6.94	-0.52	-0.18	7
AM 18C	11.70	6.95	-0.64	-0.07	7
AM 19	11.40	6.96	-0.46	-0.34	3
AM 19C	10.65	6.97	-0.65	-0.47	3
AM 20	10.10	6.98	-1.09	-1.79	4
AM 20C	9.65	7.00	-0.87	-1.00	4
AM 21	8.05	7.03	-0.99	-0.66	4
AM 22	7.10	7.05	-0.61	-0.79	4
AM 23	5.50	7.09	-1.23	-2.30	3
AM 24	3.90	7.13	-0.61	-0.55	4
AM 25	2.30	7.17	-1.20	-1.75	4

Supplementary table 4. $\delta^{13}C$ and $\delta^{18}O$ data on bulk sediments.

References

Bouchal, J.M., Güner, T.H., Velitzelos, D., Velitzelos, E., Denk, T., 2020. Messinian vegetation and climate of the intermontane Florina–Ptolemais–Servia Basin, NW Greece inferred from palaeobotanical data: how well do plant fossils reflect past environments? Royal Society Open Science 7: 192067. http://dx.doi.org/10.1098/rsos.192067

Butiseacă, G.A., Vasiliev, I., van der Meer, M.T.J., Krijgsman, W., Palcu, D.V., Feurdean, A., Niedermeyer, E.M., Mulch., A., 2021. Severe late Miocene droughts affected Eurasia. Global and Planetary Change, 206, 103644 https://doi.org/10.1016/j.gloplacha.2021.103644.

Ivanov., D.A., Ashraf, A.R., Mosbrugger, V., Palmarev, E., 2002. Miocene microflora and paleoclimate reconstructions from three sites in Bulgaria. Pangaea. https://doi.org/10.1594/PANGAEA.596352

Kontakiotis, G., Besiou, E., Antonarakou, A., Zarkogiannis, S.D., Kostis, A., Mortyn, P.G., Moisette, P., Cornée, J.-J., Schulbert, C., Drinia, H., Anastasakis, G., Karakitsios, V., 2019. Decoding sea surface and paleoclimate conditions in the eastern Mediterranean over the Tortonian-Messinian Transition. Palaeogeography, Palaeoclimatology, Palaeoecology, 534. https://doi.org/10.1016/j.palaeo.2019.109312

Kontakiotis, G., Butiseacă, G.-A., Karakitsios, V., Antonarakou, A., Zarkogiannis, S., Agiadi, K., Krsnik, E., Besiou, E., Zachariasse, J.-W., Lourens, L., Thivaiou, D., Koskeridou, E., Moissette, P., Mulch, A., Vasiliev., I., 2022. Hypersalinity accompanies tectonic restriction in the eastern Mediterranean prior to the Messinian Salinity Crisis. Palaeogeography, Palaeoclimatology, Palaeoecology 592(2):110903. https://doi.org/10.1016/j.palaeo.2022.110903

Mancini, A.M., Gennari, R., Ziveri, P., Mortyn, P.G., Stolwijk, D.J., Lozar, F., 2020. Calcareous nannofossil and foraminiferal trace element records in the Sorbas Basin: A new piece of the Messinian Salinity Crisis onset puzzle. Palaeogeography, Palaeoclimatology, Palaeoecology 554. https://doi.org/10.1016/j.palaeo.2020.109796

Mayser, J.P., Flecker, R., Marzocchi, A., Kouwenhoven, T., Lunt, D., Pancost, R., 2017. Precession driven changes in terrestrial organic matter input to the Eastern Mediterranean leading up to the Messinian Salinity Crisis. Earth and Planetary Science Letters, 462, 199-211. https://doi.org/10.1016/j.epsl.2017.01.029

Targhi, S., Barhoun, N., Taoufiq, B.N., Achab, M., Ait Salem, A., Yousfi, M.Z., 2021. Vegetation climate and marine environmental reconstruction in the western Mediterranean (southern Rifian corridor, Morocco) over the Tortonian-Messinian transition. Helyon 7, 208569. https://doi.org/10.1016/j.heliyon.2021.e08569

Tzanova, A., Herbert, T., Peterson, L., 2015. Cooling Mediterranean Sea surface temperatures during the Late Miocene provide a climate context for evolutionary transitions in Africa and Eurasia. Earth and Planetary Science Letters. 419. http://doi.org/10.1016/j.epsl.2015.03.016

Utescher, T., Djordjevic- Milutinovic, D., Bruch, A., Mosbrugger, V., 2007. Paleoclimate and vegetation change in Serbia during the last 30 Ma. Palaeogeography, Palaeoclimatology, Palaeoecology 253, 157–168. https://doi.org/10.1016/j.palaeo.2007.03.037

Vasiliev, I., Reichart, G.J., Krijgsman, W., Mulch, A., 2019. Black Sea rivers capture drastic change in catchment-wide mean annual temperature and soil pH during the Miocene-to-Pliocene transition, Global and Planetary Change, 172, 428–439. https://doi.org/10.1016/j.gloplacha.2018.10.016

Vasiliev, I., Feurdean, A., Reichart, G.J., Mulch, A., 2020. Late Miocene intensification of continentality in the Black Sea Region. International Journal of Earth Sciences, 109, 831–846. https://doi.org/10.1007/s00531-020-01832-w